HETEROGENEOUSLY ALLOYED SEMICONDUCTOR NANOCRYSTALS WITH INDUCED CHEMICAL COMPOSITION GRADIENTS

By

Melissa Ambre Harrison

Dissertation

Submitted to the Faculty of the

Graduate School of Vanderbilt University

in partial fulfillment of the requirements for

the degree of

DOCTOR OF PHILOSOPHY

in

Materials Science

December, 2012

Nashville, Tennessee

Approved by:

Professor Sandra J. Rosenthal

Professor Timothy Hanusa

Professor Bridget Rogers

Professor Sharon Weiss

Dedicated

to

my family and friends

for their unwavering encouragement and support.

ACKNOWLEDGEMENTS

First, I express my sincere appreciation to my advisor, Professor Sandra Rosenthal, for affording me the opportunity to learn and develop as both a scientist and professional. Your efforts are greatly appreciated. I am endlessly grateful.

I would also like to thank other members of my Ph.D. Committee: Professor Timothy Hanusa, Professor Bridget Rogers and Professor Sharon Weiss for their guidance and advice during my development.

Amy Ng, this would have been much more difficult without you. You helped me to make sense of my own gibberish. Thank you for all of your time and efforts. Scott Niezgoda, Joe Keen and Noah Orfield, thank you all for believing enough in my work to sacrifice your time and resources to work with me. I hope this work has been and will continue to be just as beneficial for you all.

Special thanks to the members of the Rosenthal group, past and present. I have learned more chemistry just in talking to and observing you all than I have from the few courses I've taken over the years. You all have made me a better scientist. I wish you all great success in your future endeavors. Emily Ross and Oleg Kuvton, there is something about your senses of humor that make me feel normal. Thank you for peace of mind. Jerry Chang, thank you for sharing your knowledge. Also, thank you Dr. James McBride for your timely advice.

Professor Keivan Stassun, I appreciate you for always being on my side. You have opened many doors for me and I am forever grateful. Special thanks to Professors Arnold Burger, Kelly Holley-Bockelmann, David Ernst and Dina Stroud for your continued encouragement and support. Thanks to Alyce Dobyns, Constantine Coca and the Bridge family. I would like to extend my utmost gratitude to Sarah Satterwhite for always providing reliable and unfailing support. Where would I be without you? Seriously.

Drs. Chinessa Atkins, Suseela Somarajan, Sameer Mahajan and John Rigueur, thank you all, even post-graduation, for the continued support. Jedidah Isler Gonda, your help over the years has invaluable. I am grateful to have a friend like you. Dr. Janina Jeff and Brittany Allison, thank you for helping me to preserve my sanity both on and off campus.

Family and friends, words cannot express how grateful I am to have had you by my side. Each of you has played an integral part in my development. Thank you for making me the woman I am today. Lynette, Opal, Oliver and Matthew, all of this is

because of you. Jamie, Bonnie, Erica, Greer, Kennetha, Gabby, Alisha, Joni, Jay and Shelonda, thank you all for being just what I needed when I needed it. Jamie you have truly kept me sane. Karwin, Teshad and Taurean, just knowing that you were just a phone call away has been more comforting than you know. Michael, thank you for your unrelenting support. You inspire me to new heights day by day. Thank you.

Lastly, I would like to acknowledge financial support from the National Science Foundation, I^3 Program HRD-0930018; Vanderbilt University, Provost's Fellowship; National Science Foundation, IGERT Fellows Program; the US Department of Education, GAANN Program; and the US Department of Energy, Basics Sciences Division.

TABLE OF CONTENTS

Page

LIST OF TABLES

Page

LIST OF FIGURES

Page

CHAPTER I

INTRODUCTION

1.1 Overview

We are in an age of rapidly advancing technologies. Our lives are constantly being transformed as scientific innovations continue to drive cultural shifts and shape our future. The undeniable driving force behind our improving technologies is our evolving knowledge of how to manipulate life's building blocks, atoms. Innovative materials have been the basis of innovative technologies. As eloquently stated in a publication written by Qingshan Li and associates, "Materials science is the pillar of modern science and technology, industrial production and economic life."[1] Continuing progressions in technology heavily rely on discovery and understanding of new materials and structures. Many are looking to nanoscale materials to usher in a new era of electronics.

The ability to tune and enhance the physical properties of nanomaterials is imperative to moving beyond our current capabilities to more advanced technologies. The focus of this work is on doing just that – manipulating atomic building blocks to tune and enhance the physical properties of nanomaterials. The ability to induce and vary chemical composition gradients has allowed for the discovery of a new realm of functional materials whose physical properties are governed by phenomena that we do not yet understand. In this dissertation we will explore and unveil physical properties and phenomena unique to semiconductor nanocrystals with chemical composition gradients.

1.2 Semiconductor Nanocrystals

Semiconductor nanocrystals have been utilized for the past several years due to their unique physical properties.[2] Typically, the optical and electrical properties are governed by quantum confinement effects with observed optical and electronic properties tunable with nanocrystal size[3,4,5,6,7] and morphology[8,9,10,3,11] in binary materials[12]. For this reason, semiconductor nanocrystals have been applied toward light-emitting diodes[13,14,15], photocatalysis[16,17,18,19], biological labels[20,21,22,23] and lasers[24,25].

There has been enormous growth and maturity in the field of semiconductor nanocrystals since their development more than 20 years ago. Semiconductor nanocrystals—or quantum dots—have demonstrated unique and remarkable size dependent physical properties due to the effect of quantum confinement on nanocrystals.[26,27,28,29] Quantum confinement occurs when the size and dimensions of semiconductor crystals are restricted to less than or equal to their bulk Bohr exciton (the bound state of an electron and hole carrying zero charge[30]) diameter. Quantum confinement may also occur at diameters larger than the Bohr exciton radius, but at a different degree. Increasing structural confinement typically results in increases in the band gap energy of the material. This relationship between crystal size and band gap energy allows for the tuning of band gap related absorption and luminescence by changing the crystal size.

Depending on the properties of the material, excitons can be treated in two limiting cases: [1)] Frenkel excitons and [2)] Wannier-Mott excitions. Frenkel excitons exist in materials with small dielectric constants where the Coulomb interaction between the electron and hole is typically strong resulting in smaller excitons, of the same order of

magnitude as the size of the unit cell. Binding energies for Frenkel excitions are generally between 0.1 and1Ev. Wannier-Mott excitons are described by a reduced Coulomb interation between the electron and hole resulting in a loosely bound exciton with a radius larger than the lattice spacing. These excitons are typical of semiconductor materials due their large dielectric constants. The Wannier-Mott exciton binding energy is typically much less than that of the hydrogen atom, on the order of 0.01 Ev.

For a localized electron-hole pair, the electron and hole interact via the electrostatic attraction. As any two –particle system, the exciton motion can be decomposed into two parts: a center –of-mass (CM) motion and a relative motion of the two particles about the CM. Since the coulomb interaction depends only on the relative coordinate of the electron and hole, the exciton CM behaves like a free particle with mass $M=m_e+m_h$ where m_e and m_h are the electron and hole effective masses. The relative motion of electron and hole in the exciton is similar to that of the electron and proton inside the hydrogen atom. Combining the results for the relative motion and CM motion of the exciton, the energy that is necessary to obtain the excited state (exciton energy)

$$E_{ex} = E_g + \frac{\hbar^2 k^2}{2M} - \frac{R^*}{n^2}$$

(1.1)

where E_g is the band gap energy, the second term represents kinetic energy of the translation motion that is negligible compared to electrostatic interaction energy, and the third term represents the hydrogen-like set of energy levels.

R^* is the Rydberg constant for exciton defined as

$$\frac{\mu e^4}{2(4\pi\varepsilon_0\varepsilon\hbar)^2} \qquad (1.2)$$

n is the principal quantum number and k is the exciton vector. In the hydrogen atom the radius of the most probable orbit is called Bohr radius a_o (0.53A·U). Similarly, the Bohr radius of the exciton,

$$a_B = \frac{m\varepsilon a_0}{\mu} \tag{1.3}$$

where μ is the reduced mass of exciton[31].

The situation changes in the case of nanoscale semiconductor particle with size on the order of the Bohr exciton radius. The electron hole pair energy levels in quantum dots cannot be treated further based on hydrogen model. The exciton levels are given by solving the classical quantum mechanical problem of a particle in a box. This size range corresponds to the regime of quantum confinement for which electronic excitations feel the presence of the particle boundaries and respond to changes in the particle size by adjusting their energy spectra. This is known as "quantum size effect"[32]. As the quantum dot size decreases, the energy gap increases leading to blue shifts in absorption and emission wavelengths. In addition to increasing energy gap, quantum confinement leads to a collapse of continuous energy bands of the bulk material into discrete atomic energy levels. The discrete structure of energy states leads to dominant features in the continuous absorption spectrum of QDs due to symmetry allowed transitions[32]. Since QDs are more closely related to atoms than bulk material because of their discrete, quantized energy levels, they have been nicknamed as artificial atoms.

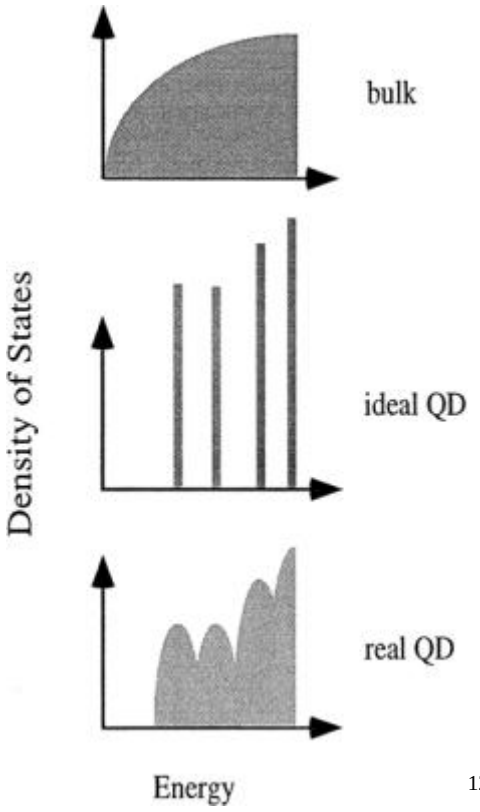

Figure 1.1 Bulk semiconductor materials have continuous conduction and valence energy bands separated by a fixed energy gap. As the size of the material decreases, energy bands collapse into more discrete, atomic-like states with energies dependent on the particle radius. The quantum dot (QD) is characterized by the effect of changing electronic structure with particle size and the resultant physical properties[32].

The most immediately obvious evidence of quantum confinement in semiconductor nanocrystals is the shift in optical absorption and emission spectra with size. An absorption event promotes an electron from valence band to conduction band, leaving a region of positive charge (hole) in the valence band. The resultant electron-hole pair is treated as an exciton due to confinement. The resultant bound electron-hole pair is an example of the particle in a box model in quantum mechanics. The basic model of the behavior of system was developed by L. E. Brus *et al*[33]. To explain the behavior of the

electron and hole in this system, Brus's model makes the following approximations of the system:

1. The nanocrystal is spherical, with a radius of R.
2. The interior of the nanocrystal is a uniform medium; there are no point charges or occupied spaces other than the excited electron and hole (i.e., nuclei or bound electrons).
3. The potential energy outside the nanocrystal is infinite; thus the electron and hole are always found within the nanocrystal (i.e., the surface of the nanocrystal defines the walls of the "box")[33b].

The Hamiltonian for a free point charge in a nanocrystal is:

$$H = -\frac{h^2}{8\pi^2 m_c}\nabla_C^2 + \tilde{V}, \quad \tilde{V} = \begin{cases} r \leq R \\ r \geq R \end{cases} \tag{1.4}$$

where m_c is the effective mass of the point charge and r is the distance from the center of the nanocrystal. The solution to the Schrödinger equation in this case is the familiar particle in-a-box solution to, modified for the case of a sphere:

$$\Psi_n(r) = \frac{1}{r\sqrt{2\pi R}}\sin\frac{n\pi r}{R} \tag{1.5}$$

$$E_n = \frac{h^2 n^2}{8 m_c R^2}; \quad n = 1, 2, 3 \ldots \tag{1.6}$$

Qualitatively, equation 1.6 illustrates the particle-in-a-box behavior of nanocrystals. As the size of the nanocrystal increases, the energy of electron in the well decreases. In reality, creation of an exciton in a nanocrystal involves two charges, the electron and the hole.

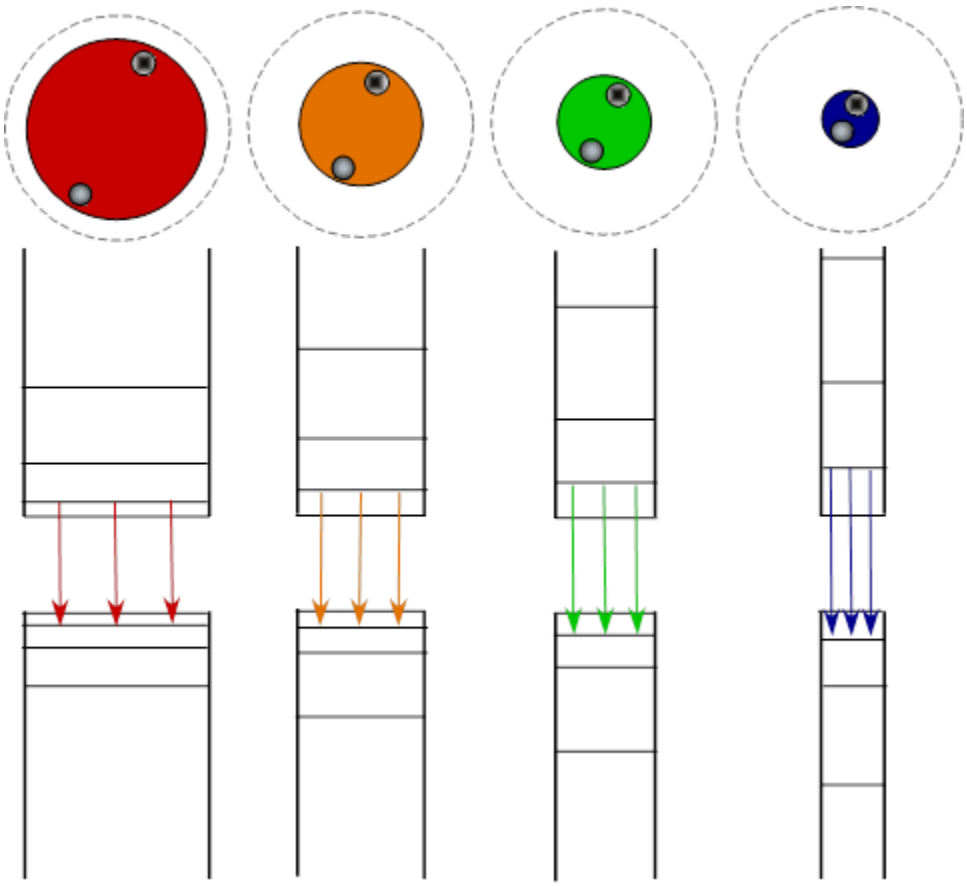

Figure 1.2 Schematic demonstrating the quantum confinement effect in semiconductor nanocrystals. Spatial confinement of carriers directly affect the electronic structure of the material. With decreasing particle size, below that of the Bohr exciton radius (shown as circles around particle depictions), blue shift in optical properties are observed and associated with widening band gap energies.

The Hamiltonian describing the case of the electron-hole pair is as follows:

$$H = -\frac{h^2}{8\pi^2 m_e}\nabla_e^2 - \frac{h^2}{8\pi^2 m_h}\nabla_h^2 + \hat{V}(\bar{S}_e, \bar{S}_h) \qquad (1.7)$$

where S_e and S_h are the positions of the electron and hole, respectively, within the diameter of the nanocrystal, m_e is the effective mass of the electron and m_h is the effective mass of the hole. The potential energy consists of two parts and is assumed infinite for $r > R$. For $r < R$ the first part is the Coulomb attraction between the negatively charged

electron and the positively charged hole and the second component is the polarization energy. Essentially, a point charge inside a nanocrystal polarizes the crystal. This polarization affects the energy of the second charge. Including the polarization effect, the total Hamiltonian

for the electron–hole system in a nanocrystal is :

$$H = -\frac{h^2}{8\pi^2 m_e}\nabla_e^2 - \frac{h^2}{8\pi^2 m_h}\nabla_h^2 - \frac{e^2}{4\pi\varepsilon\varepsilon_0|\bar{S}_e - \bar{S}_h|} + Polarization\ terms \quad (1.8)$$

As the polarization term is small compared to the kinetic and Coulomb energies, a good understanding of the lowest-energy excitonic state may be made by omitting this term. So an analytical approximation for the first excited electronic state is:

$$E = E_g + \frac{\hbar^2\pi^2}{2R^2}\left[\frac{1}{m_e} + \frac{1}{m_h}\right] - \frac{e^2}{4\pi\varepsilon\varepsilon_0|\bar{S}_e - \bar{S}_h|} + smaller\ terms \quad (1.9)$$

In this equation E_g is the band gap energy of the bulk semiconductor, the second term describes the energy due to quantum localization and the third term describes the energy due to Coulomb attraction between electron and hole. The Coulomb term shifts E to lower energy as 1/R, while the quantum localization term shift E to higher energy as $1/R^2$. Thus the apparent band gap will always increase for small enough R – an effect that has now been experimentally observed for many different materials.

1.3 Surface Passivation for Improved Optical Response

Several techniques have been employed to produce nanocrystals that demonstrate high luminescent efficiency and photostability via enhanced surface passivation by using organic and inorganic capping agents[34,35]. More recently, studies have shown that capping or shelling nanocrystals with a different, albeit compatible, inorganic material results in increased quantum yields[36,12], augmented photostability[37] and blinking suppression[38,12]. These materials are referred to as core/shell nanocrystals. Core/shell materials demonstrate improved, yet less than ideal, optical properties. Though passivation of the nanocrystal surface with inorganic materials offers drastic improvements, photostability and blinking are still concerns, as well as sub-unity quantum yields[39,40]. The phenomena of enhanced optical properties in these materials are thought to be due to the smoothing of the core/shell interface by using like materials which also result in a gradually changing energy band diagram which progresses from a smaller energy band gap, due to the core material, to a wider energy band gap associated with surface structures and stoichiometry.[41] These nanocrystals were fabricated in the same way as typical core/shell materials; the difference lies in the selection and structural compatibility of core and shell materials. The use of similar materials, particularly those exhibiting the same crystal structure and only small differences in lattice constant, is thought to rectify the issue of carrier trapping in core/shell nanocrystals. Carrier trapping can arise from an abrupt core/shell interface of dissimilar materials and reduce non-radiative processes which is expected to rectify the deterrents associated with surface passivation, surface defects and defects at the core-shell interface[40]. We anticipate that gradient semiconductor nanocrystals will soon outperform traditional core/shell

nanocrystals in luminescence efficiency and photostability. More detailed discussions regarding the unique phenomena observed in gradient nanocrystals and their potential will ensue in the text to follow.

1.4 Semiconductor Alloys

Although semiconductor nanocrystals have been deemed promising materials for the aforementioned applications, attempts to fabricate nanocrystals with tunable and enhanced optical properties continue. Modifying the size of the nanocrystal is one means of tuning their optical properties. Another way would be to adjust constituent stoichiometries of alloyed semiconductors.[42,43,44,45] The alloying of two semiconductor materials in the nano-regime produces optical properties that are composition-dependent and size-dependent; the product is a material possessing distinct properties than those of their bulk, parent semiconductors. Since the optical properties depend on the constituent composition, it is possible to tune the band gap energy while maintaining particle size.[46] Alloy nanocrystals can be classified as (1) homogeneous[47,44], having a uniform internal structure or as (2) gradient where alloy compositions and structures are varied radially[48,49,50]. Researchers have been successful in fabricating both types of alloy nanocrystals as II-IV[51,42] and III-V[52,53] semiconductors.

1.5 Nanocrystal Alloys with Chemical Composition Gradients

Semiconductor alloys that demonstrate chemical composition gradients are described as alloy materials with depth-dependent and progressive stoichiometries. In the case of gradient semiconductor alloys, chemical stoichiometries progressively vary with radius.

These materials are similar to multi-layered materials composed of alloys with the same atomic components but continually increasing or decreasing atomic ratios per layer. In the case of gradient nanomaterials, these "layers" are close to immeasurable due to the Angstrom thin depths and the absence of technology to effectively probe the radially fleeting stoichiometries.

In 2008, Chen et al. reported the synthesis of "giant" nanocrystals of single-component—CdSe/19CdS and of multi-component—CdSe/11CdS-6Cd_xZn_yS-2ZnS10[54]. Though these materials demonstrate suppressed blinking as a result of their multi-shell configuration, a 30% reduction in quantum efficiency was also reported. Also in 2008, Bae *et al.* reported the synthesis and characterization of compositionally gradient CdZnSSe nanocrystals with emission intensities of 80%.[48] Bae *et al.* also went on to demonstrate the functionality of these materials by incorporating the gradient nanocrystals into light emitting diodes.[13a] This work has since been overshadowed by Wang et al. in 2009 with reports of non-blinking CdZnSe/ZnSe graded nanocrystals, though the quantum efficiency of these nanocrystals were only 50%[55]. Using electron microscopy techniques, McBride *et al* investigated the correlation between lattice strain, surface passivation and quantum efficiencies in multi-shell CdSe/CdS/ZnS nanocrystals with quantum efficiencies of 84%[56]. Though fabricated as core/shell nanoparticles, the multi-shell structure along with the choice in compatible materials facilitates gradient-like configurations resulting in improved photophysical properties.

There are not many reports describing the differences in physical properties of compositionally gradient nanocrystals compared to currently employed configurations such as core/shell materials. Though similar in nature, these materials are a step beyond

that of core/shell materials. In inducing chemical composition gradients, "core" materials, which are primarily responsible for the resultant physical properties of the gradient unit, are seamlessly encapsulated. The functionality of the gradient unit can not only be manipulated by varying the degree of gradation of the material but also in appropriately choosing shell materials. Just as core/shell materials are classified by many types, several classifications of gradient materials are possible.

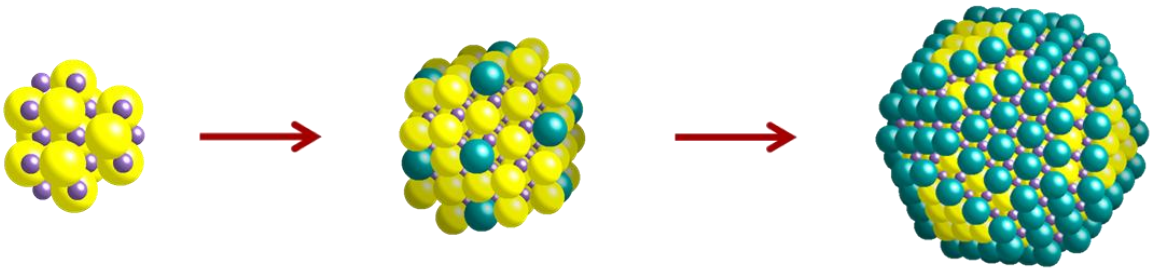

Figure 1.3 Schematic depicting the progression of growth for nanocrystals with chemical composition gradients where chemical compositions vary progressively with nanocrystals radius.

1.6 Scope of this Work

This document depicts the development process for CdSSe semiconductor nanocrystals with chemical composition gradients and unveils their unique photophysical properties through a series of characterization techniques probing stoichiometries, structures, morphologies and optical properties. Chapter II begins describing the factors considered in developing our synthetic technique to manipulate induced chemical composition gradients and probe the effects of varying degrees of gradation on the resultant photophysical properties. This chapter continues with a description of synthetic procedures employed and techniques used for the characterization of gradient nanocrystals. As-synthesized CdSSe nanocrystals and the results of our experiments are

presented in Chapter III. Discussions regarding the gradient nature of CdSSe nanocrystals and the effects of varying synthetic parameters on photophysical properties are included in Chapter III.

Finally, a chapter is presented which summarizes the accomplishments of this work; also included are suggestions for its future. This work was intended to seed future studies and discussions regarding the effects of inducing chemical composition gradients in alloy materials on the resultant physical properties. The appendix provides data from experiments with additional gradient nanocrystal chemistries.

CHAPTER II

EXPERIMENTAL METHODS

2.1 Synthetic Considerations for Nanocrystals with Chemical Composition Gradients

In this work, we present the synthesis and optical characterization of compositionally graded CdSSe nanocrystals. In producing ternary materials by colloidal means, there are several possible routes to induce homogeneity or inhomogeneity in chemical composition. In the work presented by Swafford *et al.* on the synthesis, characterization and growth kinetics of homogeneously alloyed cadmium sulfoselenide (CdS_xSe_{1-x}), the authors reported an observation in the differences in reactivity of bound and unbound sulfur precursors; in particular, sulfur bound by excess tributylphosphine compared to elemental sulfur[51]. In comparison, unbound sulfur precursors produced homogeneous ternary alloys, and bound sulfur precursors produced an inhomogeneous ternary structure with a composition gradient. The ratio of the rates of addition of sulfur and selenium is proportional to the rates of concentrations of sulfur and selenium:

$$\frac{\frac{d[AS-S]}{dt}}{\frac{d[AS-Se]}{dt}} = \frac{k_1[AS][S]}{k_2[AS][Se]} = \frac{k_1[S]}{k_2[Se]} \tag{2.1}$$

where *AS* is an available anion binding site and k_1 and k_2 are rate constants. Bound sulfur precursors facilitated delayed incorporation of sulfur into the nanocrystal matrix, resulting in materials with gradually increasing concentrations of sulfur. Here, we make use of this synthetic approach which exploits the differences in reactivity of each anionic

precursor where $k_1 \neq k_2$ and [S] ≠ [Se]. We also consider the Arrhenius equation which describes the temperature dependence of rate constants and

$$k = Ae^{-E_{\propto}/RT} \quad (2.2)$$

where A is the prefactor related to the frequency of molecular collisions, $E_{\propto}$ is the activation energy and R is the universal gas constant. Variation in growth temperature to alter the degree of gradation and changes in optical properties in compositionally graded nanocrystals is also reported.

There are many parameters associated with colloidal techniques capable of disturbing the anticipated effect of inhomogeneity of a ternary alloy which we have taken into consideration. The hot-injection method is typically performed by injecting precursor materials at an elevated temperature followed by growth at a significantly lower temperature[57]. To avoid alloyed nucleation, injection of precursors and growth were carried out at the same temperature. Furthermore, to avoid fluctuations in temperature due to injection, high concentration precursors were used to decrease the volume size of injection fluids and reduce temperature perturbations during the reaction.

Materials. Cadmium oxide (CdO, 99.99%), zinc acetate 15ehydrate [$Zn(Ac)_2 \cdot 2H_2O$, 99.99%], lead acetate trihydrate [$Pb(Ac)_2 \cdot 3H_2$), 99.999%], oleic acid (OA, 90 %), octadecene (ODE, 90%) and tri-n-butylphosphine (TBP, 93%) were purchased from Sigma Aldrich. Elemental selenium (Se, 99.99%) was purchased from Strem. Sulfur powder (USP sublimed) was purchased from Fisher Scientific. A concentrated selenium stock solution (2 M) was prepared by dissolving 1.58 g of Se in 10 Ml of TBP. The sulfur stock solution was prepared by dissolving 0.64 g of sulfur in 10 Ml of TBP. Both

stock solutions were diluted to 0.75 M in ODE. Injection solutions were prepared by mixing the desired ratio of both S and Se stock solutions.

2.2 Nanocrystal Synthesis

2.2.1 CdSSe Nanocrystals

The synthesis of compositionally graded CdSSe nanocrystals[58] was carried out by loading 1 mmol of CdO, 4 mmol of OA and 20 Ml ODE into a 100 Ml, 3-neck round bottom flask and heating to 220°C under argon flow. With heating, a colorless Cd-oleate complex is formed. Mixed injection solutions of 0.8x Ml of 0.75 M Se: TBP in ODE and 0.8(1- x) Ml of 0.75M S: TBP in ODE, both with 60% TBP, were then injected into the flask. Nanocrystals were allowed to grow for up to 2 hours, and then cooled to below 100°C. During growth, aliquots of the CdSSe nanocrystals were taken at varying time intervals. A mixture of butanol and ethanol were used to precipitate the synthesized nanocrystals and the mixture was centrifuged for 20 minutes at 7500 rpm. Subsequent cleaning was performed by suspending the nanocrystal pellets in hexanes, and then precipitating with the addition of ethanol. Mixtures were then centrifuged for 5 minutes at 10,000 rpm. This cleaning step was repeated three times. Nanocrystals were then dispersed in hexanes. Rutherford backscattering spectroscopy was used to probe the discarded supernatant and confirmed that the cleaning procedure used was sufficient to remove the remaining precursor materials. An image of the synthesis set up is shown in Figure 2.1.

Figure 2.1 Image of nanocrystal synthesis setup. The 3-neck flask was seated atop a stir plate inside a heating mantle, heated to the appropriate reaction temperature. Reaction temperatures are varied by using a digital temperature controller, which is connected to the heating mantle, to set the desired temperature. A thermocouple is also attached to the temperature controller and inserted into the reaction flask to monitor the temperature of the solution. A stir bar was placed inside the flask and stirred rapidly to help maintain a uniform temperature throughout the solution, as well as uniform concentration of reactants. A rotary evaporator, bump trap is inserted into the center neck of the reaction flask and is attached to an argon bubbler to allow the nanocrystal synthesis to occur in an environment free of water and oxygen. The remaining neck is fitted with a rubber septum to close off the reaction to the external environment and maintain synthesis conditions. This neck is also utilizing during anionic precursor injections via syringe.

2.2.2 CdZnSe Nanocrystals

The synthesis of compositionally graded CdZnSe nanocrystals was carried out by loading 0.5 mmol of CdO, 0.5 mmol $Zn(Ac)_2 \cdot 2H_2O$, 4 mmol of OA and 20 Ml ODE into a 100 Ml, 3-neck round bottom flask and heating to 240°C under argon flow. With heating, colorless metal oleates Cd and Zn were formed. A 1 Ml injection solution 0.75 M Se: TBP in ODE with 60% TBP was then injected into the flask. Nanocrystals were allowed to grow for 2 hours and 20 minutes then cooled to below 100°C. Aliquots of the growing CdZnSe nanocrystals were taken at varying time intervals. A mixture of butanol and ethanol were used to precipitate the synthesized nanocrystals and the mixture was centrifuged for 20 minutes at 7500 rpm. Subsequent cleaning was performed by suspending the nanocrystal pellets in hexanes, and then precipitating with the addition of ethanol. Mixtures were then centrifuged for 5 minutes at 10,000 rpm. This cleaning step was repeated three times. Nanocrystals were then dispersed in hexanes. Rutherford backscattering spectroscopy was used to probe the discarded supernatant and confirmed that the cleaning procedure used was sufficient to remove the remaining precursor materials. More on this material can be found in the Appendix A1.

2.2.3 CdPbSe Nanocrystals

CdPbSe nanocrystals were synthesized by loading 0.5 mmol of CdO, 0.5 mmol $Pb(Ac)_2 \cdot 2H_2O$, 4 mmol of OA and 20 Ml ODE into a 100 Ml, 3-neck round bottom flask and heating to 225°C under argon flow. Colorless metal oleates Cd and Pb were formed. A 1 Ml injection solution 0.75 M Se: TBP in ODE with 60% TBP was then injected into the flask. Nanocrystals were allowed to grow for 2 hours and 20 minutes

then cooled to below 100°C. Aliquots of the growing CdPbSe nanocrystals were taken at varying time intervals. A mixture of butanol and ethanol were used to precipitate the synthesized nanocrystals and the mixture was centrifuged for 20 minutes at 7500 rpm. Subsequent cleaning was performed by suspending the nanocrystal pellets in hexanes, and then precipitating with the addition of ethanol. Mixtures were then centrifuged for 5 minutes at 10,000 rpm. This cleaning step was repeated three times. Nanocrystals were then dispersed in hexanes. Rutherford backscattering spectroscopy was used to probe the discarded supernatant and confirmed that the cleaning procedure used was sufficient to remove the remaining precursor materials. More on this material can be found in the Appendix A2.

2.3 Characterization Techniques

2.3.1 Size and Morphology

Due to the inherent effects of morphology and size on the optical properties of nanocrystals, it was imperative to first determine the sizes and shapes of synthesized materials. High-resolution transmission electron microscopy (HR-TEM) was used to image the nanoscale materials. In this technique, a beam of electrons is transmitted through an ultra-thin sample and interacts with the sample as the beam conveyed. Due to this, an image is formed and detected. For these experiments, images were collected by a charge-couple device (CCD) camera in which the movement of electrical charge is manipulated and converted into a digital image.

TEMs are capable of producing high resolution images of nanocrystalline materials owing to the small de Broglie wavelength of electrons. This enables observation of fine detail – even as small as rows of atoms, which make up fringe patterns visible in TEM images of nanocrystalline materials, and even a single column of atoms on the Angstrom scale. The contrast visible in TEM images is due to absorption of the electrons in the material as a result of the thickness and composition of the sample.

High resolution transmission electron microscopy (HR-TEM) was performed using a Philips CM20 TEM operating at 200Kv. HR-TEM samples were prepared by drop casting clean nanocrystals suspended in hexanes onto an ultrathin carbon-on-Formavar TEM grid (Ted Pella, Inc.). Images were used to observe morphology and the dispersivity of the nanocrystals.

2.3.2 Crystal Structure

Crystalline structures of compositionally graded nanocrystal samples were determined using powder X-ray diffraction (XRD). This technique is based on observations of scattered intensities of an x-ray beam impinging on the sample as a function of incident angle and scattering angle, polarization, and wavelength. This technique is typically employed to investigate the crystalline structure of materials with long-range order (i.e. bulk materials). Because of their small size, nanocrystals are considered to have short range order and produce increasing values of the breadth of the diffraction peaks are observed with decreasing nanocrystal diameters. Paul Scherrer describes the breadth of a diffraction peak as being the width of the peak maximum at

half its height. The breadth of a diffraction peak is also affected by the size distribution of the crystallites, or the range of order (equation 2.3).

$$\varepsilon = \frac{\lambda}{\beta \cos \theta} \tag{2.3}$$

where ε is the apparent crystallite size, λ is the radiation wavelength, β is the line broadening at half maximum intensity (radians) and θ is the Bragg angle. The 'true' size (p) of the crystallite is given by

$$p = K\varepsilon \tag{2.4}$$

where K is a dimensionless number, known as the Scherrer constant, dependent on the crystallite shape and crystallite-size distribution[59]. For spherically shaped crystallites, $K_\beta = 1.0747$.[59]

XRD spectra were acquired using a Scintag X_1 θ/2θ automated powder X-ray diffractometer with a Cu target (λ = 1.54056 Å), a Peltier-cooled solid-state detector, and a zero-background, Si (5 1 0) substrate. Once cleaned, nanocrystals were suspended in hexanes solutions and drop cast onto the Si substrate for analysis.

2.3.3 Elemental and Stoichiometric Analysis

Rutherford backscattering spectrometry (RBS), or sometimes referred to as high-energy ion scattering, is an analytical technique used in materials science to determine the structure and composition of a sample by measuring backscattered ions of high energy impinging on the sample. This technique can be described as one that measures elastic collisions between and incident beam of high kinetic energy particles and the stationary particles of the sample. RBS is an extremely sensitive analytical technique in that it is capable of detecting the presence of atoms in picomolar quantities[60]. For this reason, it

was imperative to thoroughly clean nanocrystal samples to remove excess ligands and unreacted precursors.

RBS was achieved with a custom-built particle accelerator. Using a 2.0 MeV Van de Graaf generator, a gas source of helium was ionized and energized to provide the incident beam of ^{4}He ions. Experiments were performed in a high vacuum chamber ($<10^{-6}$ torr) with ^{4}He ions accelerated with energies of 1.8 MeV at normal incidence. This is depicted in the schematic shown in Figure 2.2. The ^{4}He ion beam was then directed down the beam line with magnets and through a 2 mm aperture to the target. A current around 10 Na, measured at the target, was maintained throughout the experiment to ensure sufficient data collection. Samples were prepared by drop casting a hexanes solution of nanocrystals onto the surface of a pyrolytic, graphite substrate produced by Carbone of America. Backscattered ions were collected at an angle of 176°. Resultant data was of the form of the number of backscattered ions (counts) as a function of energies of the backscattered ions (channel). This experiment displayed Poisson counting statistics where the error in the number of counts was equivalent to the square root of the number of counts[61]. A typical RBS spectrum can be seen in Figure 2.3. A spectrum of a bismuth standard is taken at the beginning of the experiment for later analysis. Analysis of the elemental composition of the nanocrystals was performed according to Feldman et al.[62]

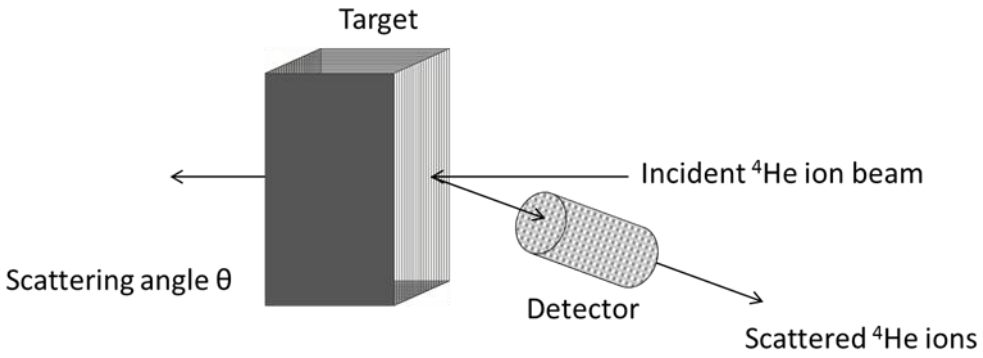

Figure 2.2 Schematic depicting RBS analysis technique.

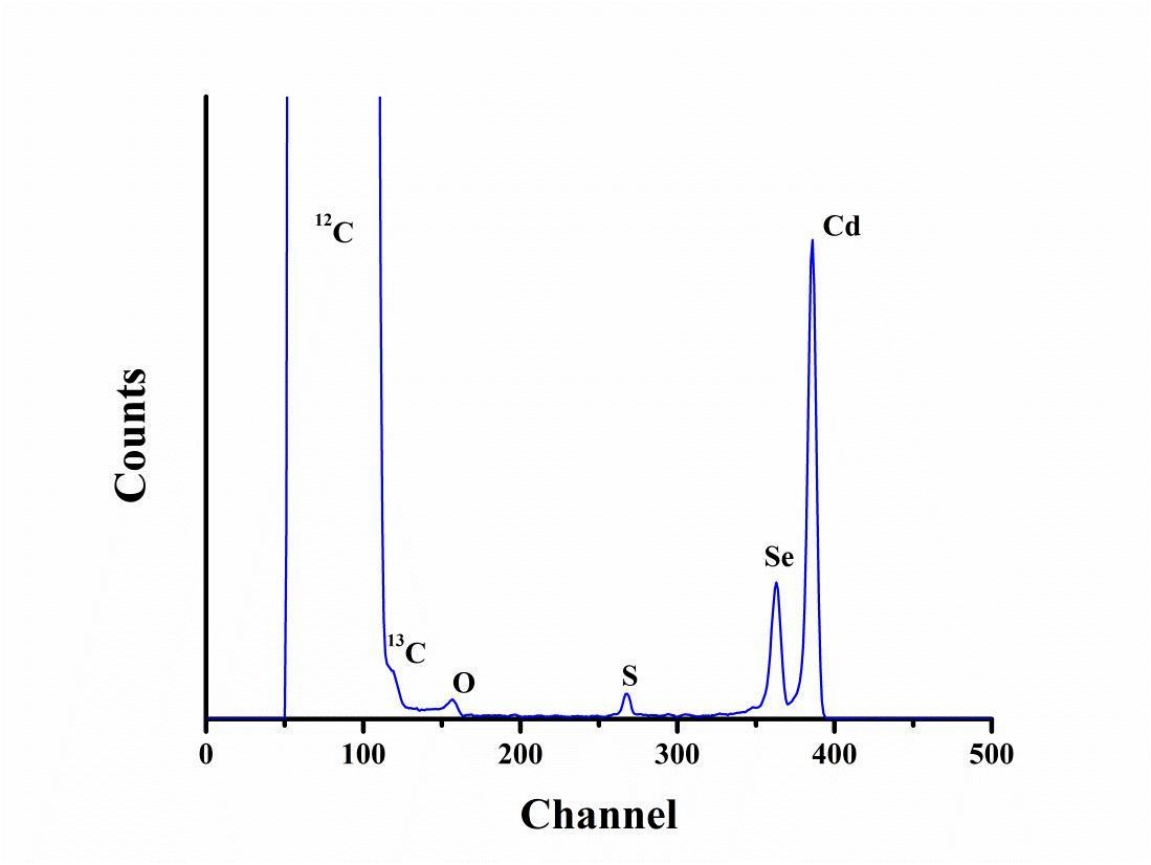

Figure 2.3 Typical spectrum obtained from RBS for semiconductor nanocrystals. The x-axis represents channel number which is proportional to the energy of backscattered ions.

Areal densities of the isolated Gaussian peaks of resultant RBS spectra were determined using the following equation (2.5):

$$N_x = \frac{(A_x)(DTR)(C_{Bi})e}{(Q)(\Omega)\left(\frac{\sigma}{\sigma_R}\right)_x(\sigma_x)} \tag{2.5}$$

where N $\left(\frac{atoms}{cm^2}\right)$ is the areal density; A is the area under the peak; DTR is the dead time ratio, calculated by dividing the 'true time' by the 'live time' particular to each experiment (DTR > 1); C_{Bi} is the bismuth correct factor which is assumed to be 1; *e* is the fundamental charge of an electron in Coulombs; *Q* is the integrated charge in Coulombs, particular to each experiment; Ω is the detector solid angle in steradians, determined using the bismuth standard; $\left(\frac{\sigma}{\sigma_R}\right)_x$ is the non-Rutherford correction factor which corrects for deviations of the cross-sections due to the influence of the nuclear force at high energies (non-Rutherford scattering or forward scattering) and is described by equation 2.6,

$$\left(\frac{\sigma}{\sigma_R}\right)_x = 1 - \frac{0.049 Z_{ion} Z_x^{\frac{4}{3}}}{E_{lab}} \tag{2.6}$$

where Z_{ion} is the atomic number of the backscattered ion and Z_x is the atomic number of the target element, and E_{lab} is the energy of the ion beam in keV (here, E_{lab} = 1800 keV); σ_x is the Rutherford cross-section for element *x* and calculated using the following equation (2.7):

$$\sigma_x = \frac{(\sigma_R)_x}{E_{lab}^2} \times 10^{-24} \tag{2.7}$$

and $(\sigma_R)_x$ is the differential cross-section in the laboratory system for element *x* and given by equation 2.8,

$$(\sigma_R)_x = \left[\left(\frac{Z_{ion}Z_x e^2}{4E_{lab}}\right)^2\right] \times \frac{4\left[\sqrt{m_x^2 - m_{ion}^2 sin^2\theta} + m_x \cos\theta\right]^2}{m_x sin^4\theta \sqrt{m_x^2 - m_{ion}^2 sin^2\theta}} \quad (2.8)$$

where m_{ion} is the mass of the backscattered ion and m_x is the mass of the target element, and θ is the backscatter angle (here, θ = 176°).

Equation 2.4 was arranged to solve Ω based on the RBS spectrum obtain for the bismuth standard. The detector solid angle was calculated by using the known value for the areal density of the standard $\left(N_{Bi} = 4.77 \times 10^{15}\ \frac{atoms}{cm^2}\right)$, using experimental values for *DTR* and A_{Bi} , and including the bismuth mass and atomic number where appropriate. The value for Ω was then used to calculate areal densities from RBS spectra of nanocrystal samples.

Considering that equations 2.5 and 2.7 rely on the mass and atomic number of element *x*, it is necessary to correctly identify elemental peaks in the obtained RBS spectra. To do so, the linear relationship between channel numbers (along the *x* axis) and energies of backscattered ions was utilized. Channel numbers had to be converted to energy values. The following equation (2.9) represents the linear relationship between channel number (N_{ch}) and energy I:

$$E = mN_{ch} + b \quad (2.9)$$

Having some knowledge of the elemental components of the sample, two peaks of the RBS spectrum were identified (i.e. the heaviest element used during synthesis and the leading edge of the carbon plateau, associated with the graphite substrate). Kinematic factors (K_x) for each element were calculated using equation 2.10,

$$K_x = \left[\frac{\sqrt{m_x^2 - m_{ion}^2 sin^2\theta} + m_{ion}\cos\theta}{m_x + m_{ion}}\right]^2 \quad (2.10)$$

and corresponding energy values were determined using equation 2.11,

$$K_x = \frac{E_x}{E_{lab}} \quad (2.11)$$

where E_x is the energy of the ions backscattered by element *x*. Once the kinematic factors and corresponding energies are identified for the known elements, the slope of the line (*m*) and y-intercept (*b*) could be calculated and the linear relationship (Eq. 2.8) particular to each RBS spectrum established for identification (or verification) of elements present in each sample.

2.3.4 Photophysical Properties

Absorption spectroscopy was used to gauge the absorption of radiation of nanocrystal samples as a function of wavelength. A generated beam of radiation is directed at the sample and transmitted radiation is detected. The obtained absorption spectrum is the fraction of incident material absorbed over a range of wavelengths. Absorption spectra were obtained with a Varian Cary 5000 UV-Vis-NIR spectrophotometer. Cleaned nanocrystal solutions were injected into a glass cuvette with a 1-cm path length for absorption and photoluminescence experiments.

Resultant absorption spectra for nanocrystal samples contain at least one initial excitonic peak and continue towards shorter wavelengths with increasing optical densities. For direct band gap semiconductor materials, this initial absorption peak represents the longest wavelength (or lowest energy) of initial photoexcitation, where electrons in the sample are excited due to the absorption of energetic photons. Relaxation

of the electrons from their excited state results in the emission of longer wavelength (or lower energy) photons. Emissions are observed in photoluminescence experiments, as described below.

Photoluminescence occurs when an electron is promoted to a higher energy state by photon absorption and then returns to a lower energy state with emission of a photon. Due to the unique optical properties exhibited by semiconductor nanocrystals, photoluminescence has become a critical characterization tool in studying the physical properties of quantum dots. Photoluminescence excitation is a complimentary technique that gauges the electronic structure of the sample, in which the wavelength of excitation is varied while the typical emission wavelength for the sample is monitored. Photoluminescence excitation spectra often mimic absorption lines of the sample. Photoluminescence (PL) and photoluminescence excitation (PLE) spectra were obtained using a Jobin Yvon Fluorolog-3 instrument, immediately following absorption spectroscopy measurements. Nanocrystal solutions with optical densities in the range of 0.8 – 1.0 were used for PL and PLE experiments.

Quantum yield values were obtained using the following equation 2.12:

$$Q = Q_R \frac{I}{I_R} \frac{OD_R}{OD} \frac{n^2}{n_R^2} \tag{2.12}$$

where Q is the quantum yield, I is the integrated intensity of the emission peak, OD refers to the optical density of the measure sample and n is the index of refraction. The subscript R denotes a reference fluorophore of known quantum yield. Rhodamine 6G (Q_R = 94% in methanol)[63] was used as a reference for quantum yield calculations of CdSSe gradient nanocrystals. Excitation wavelengths of both sample and reference were

identified by observing common absorption wavelengths and equivalent optical densities. The ideal optical material has a quantum yield of 1 (or 100%).

CHAPTER III

RESULTS AND DISCUSSION

3.22 Alloyed CdSSe Nanocrystals with Chemical Composition Gradients

3.22.1 Stoichiometric Variances in CdSSe Nanocrystals

RBS was used to gauge progressions in stoichiometric ratios of elemental components in CdSSe nanocrystal samples throughout growth. As depicted in Figure 3.1a, Cd compositions remained relatively constant and in excess[64] throughout growth, whereas Figure 3.1b demonstrates progressive incorporation of S into the nanocrystal structure. These materials crystallize with CdSe cores and gradually integrated S with growth time. Figure 3.1c illustrates this growth mechanism.

3.22.2 Nanocrystal Structure and Morphology

The crystal structure of these materials has been determined by data shown in Figure 3.2a; CdSSe nanocrystals crystallize in the zinc-blende structure. Peaks of the XRD spectra representing compositionally graded CdSSe nanocrystals are inbetween that of zinc-blende CdSe and zinc-blende CdS. These results are similar to XRD spectra of core/shell nanocrystals[65], which are an intermediate between the core and the shell, and that of pseudobinary alloys[51] which exhibit spectra between that of relative binary structures. Figure 3.2b depicts the divergence of calculated lattice constants (*a*) from that

of the dominant crystal structure, bulk CdSe at a = 6.050 Å. Lattice constant values were calculated from the (1 1 1), (2 2 0) and (3 1 1) diffraction peaks with increasing S

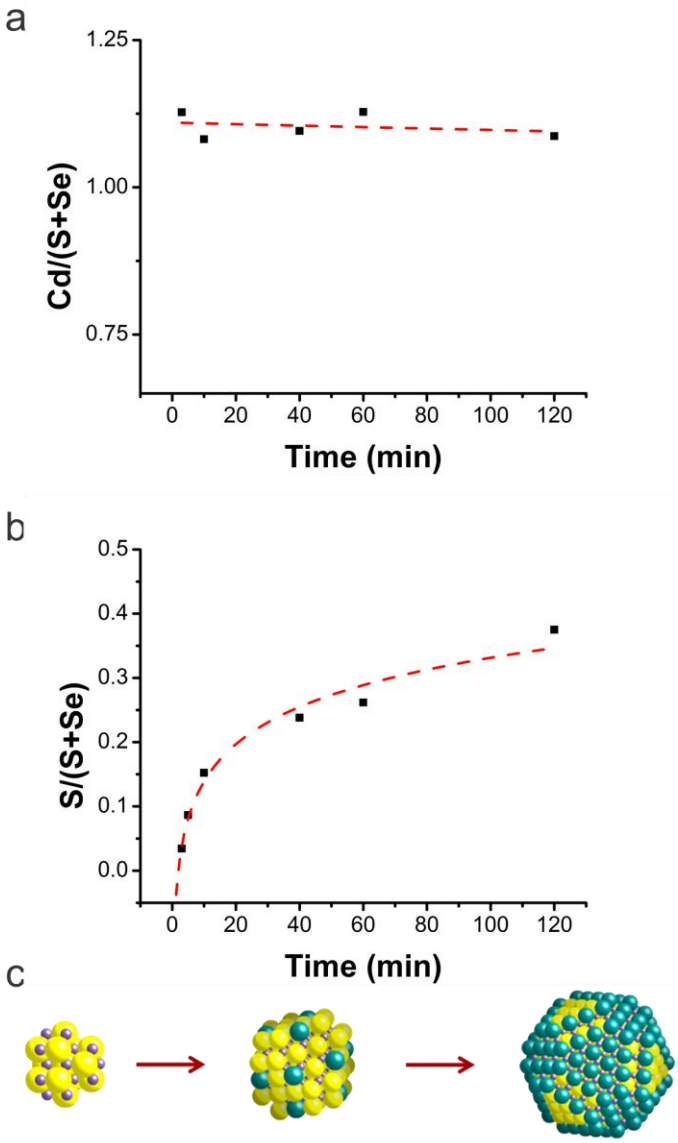

Figure 3.1 RBS analysis of nanocrystal stoichiometry as a function of growth time for CdSSe nanocrystals. Graphs depict changing chemical composition of (a) Cd[64] and (b) S and Se with growth time. The gradual increase in sulfur content with growth time indicates that these CdSSe nanocrystals are grown with a chemical composition gradient where there is a Se-rich core and S-rich shell. (c) Schematic of proposed growth of CdSSe nanocrystals with a chemical composition gradient.[58]

stoichiometries. This data also demonstrates distortions in the unit cell of the compositionally graded nanocrystals with increasing S concentrations, resulting in a modified cubic, zinc-blende structure. Lattice constants calculated using diffraction data based on the (1 1 1) diffraction peak show a gradual decrease whereas lattice constant calculations based on the (2 2 0) and (3 1 1) diffraction peaks demonstrate an initial increase then decrease in lattice constant values. These observations deviate from the typical behavior of semiconductor alloys characterized by Végard's law[66,67] which states that lattice constants change linearly with composition. Figure 3.3 is included as a visual description of the atomic arrangement for the zinc blende structure and to depict the atomic arrangement for the aforementioned diffraction planes. In early stages of growth, anomalous diffraction peaks are observed (Figure 3.4a) which are not associated with bulk CdSe or bulk CdS but may be a feature due to distorted surface atoms in ultrasmall nanocrystals. This peak diminishes with longer growth times. Similar, non-indexed peaks are observed in the literature for ultrasmall, CdSe nanocrystals[68]. Considering surface atoms are dominant in ultrasmall nanocrystals, the anomalous peak may be a feature of, and further evidence to, distorted crystal structures on the surface of these nanocrystals. With progression in growth time, the emergence of another diffraction peak is evidenced in Figure 3.4b. Although not a direct correspondence to bulk CdS, this peak is suspected to be due to the S-rich surface of the compositionally graded CdSSe nanocrystals and indicative of the progression towards a CdS surface with continued growth. The divergence of this peak from bulk CdS XRD spectra is likely due to lattice strain associated with the nano-sized (or sub-nano) thickness of the alloyed layers that construct the gradient nanocrystals. Figure 3.5 depicts non-uniform variances in fwhm of

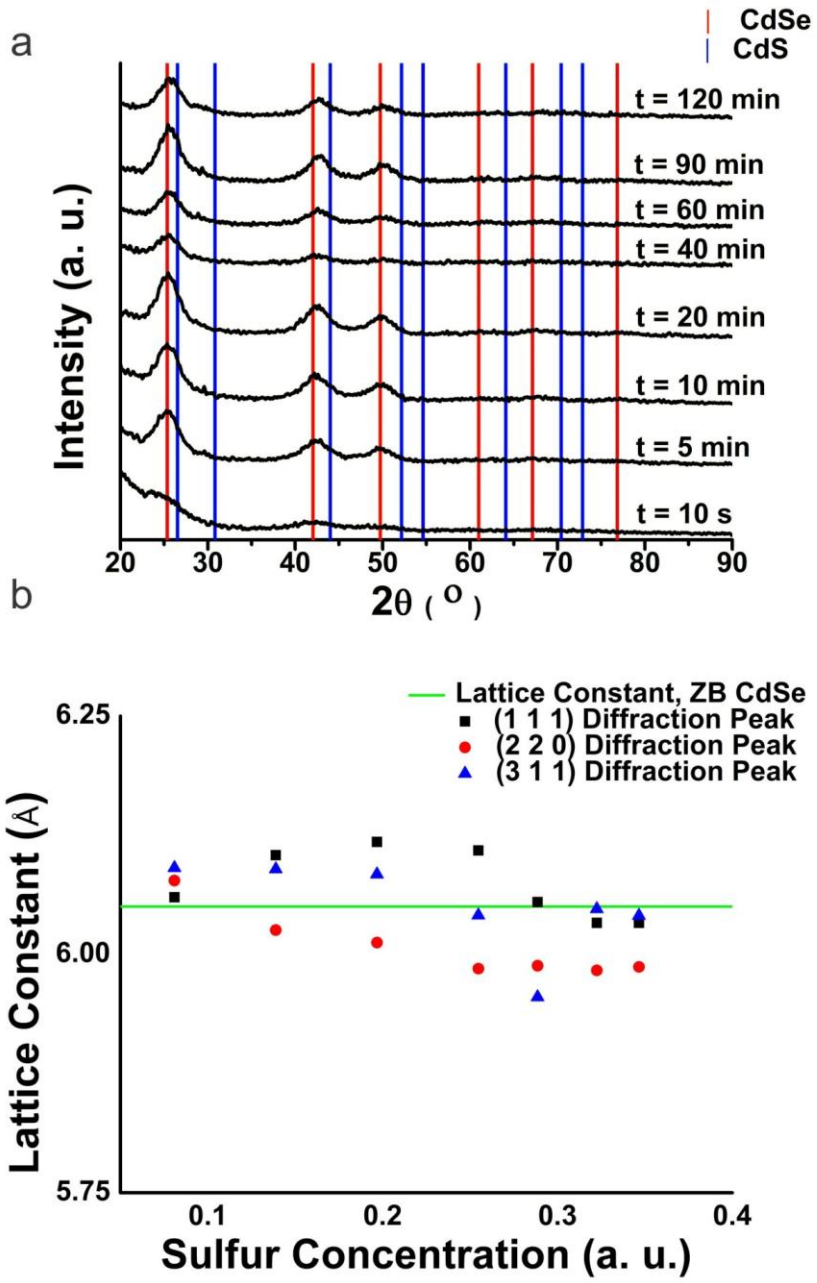

Figure 3.2 (a) XRD spectra of CdSSe nanocrystals with growth time. The spectra characterize a zinc-blende structure. (b) Plot depicting structural fluctuations in compositionally graded CdSSe nanocrystals based on lattice constants calculated from the (1 1 1) [■], (2 2 0) [●] and (3 1 1) [▲] diffraction peaks with increasing sulfur concentrations.[58]

x-ray diffraction peaks with increased growth time. This effect is referred to as line broadening.[69] This occurrence is likely due to non-uniform strain[70,71] associated with the inhomogeneous chemical composition.

High resolution transmission electron microscopy (HR-TEM) was used to determine nanocrystal sizes and morphology of as-synthesized CdSSe nanocrystals with chemical composition gradients (Figure 3.6). Aliquots taken after ~10s are approximately 1.6 nm in diameter with a 6% size distribution. Aliquots taken at 5 and 10 minute intervals are approximately 3.5 nm in diameter with 12.3% and 11.25% size distributions, respectively. Subsequent time intervals produced 4.1 nm nanocrystals with size distributions in the range of 11.6% - 14.5%. Figure 3.7 depicts the relationship between growth time, nanocrystal diameter, size distribution and sulfur concentration.

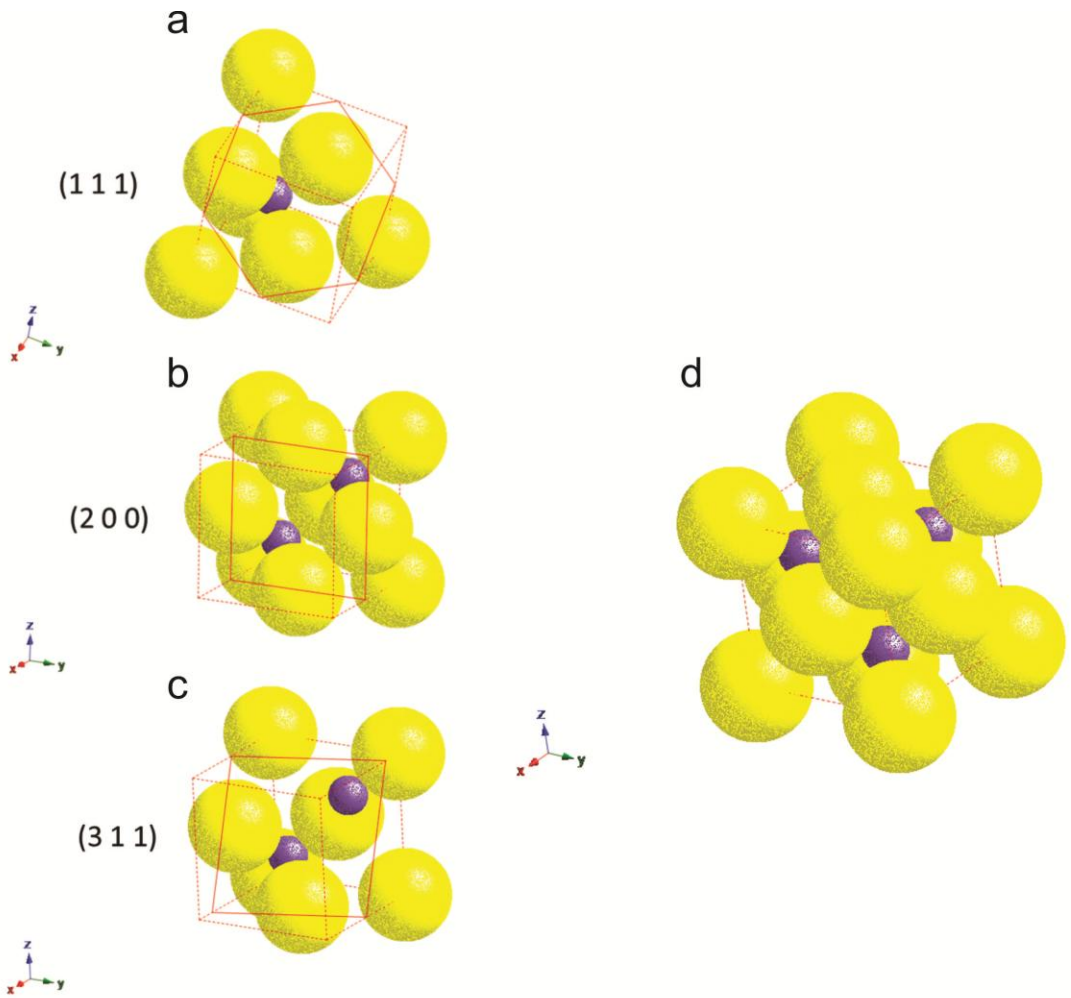

Figure 3.3 (a) Depiction of the binary zinc blende structure with a 1:1 anion to cation ratio. Cross-sections of the (1 1 1) [b], (2 0 0) [c] and (3 1 1) [d] planes are also shown.

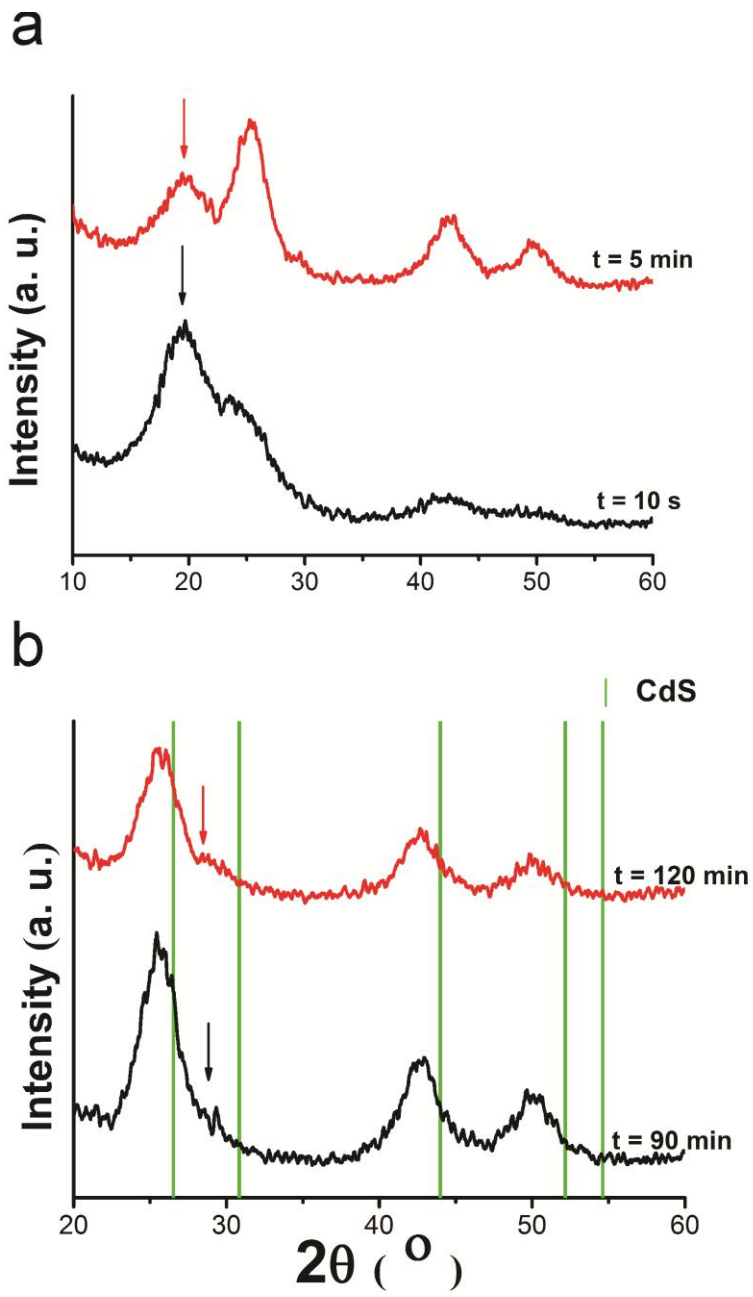

Figure 3.4 (a) In early stages of growth, anomalous diffraction peaks are observed which are not associated with bulk CdSe or bulk CdS but may be a feature due to distorted surface atoms in ultrasmall nanocrystals. (b) Diffraction peaks emerging in later stages of growth are attributed to the (2 2 0) diffraction peak of CdS.[58]

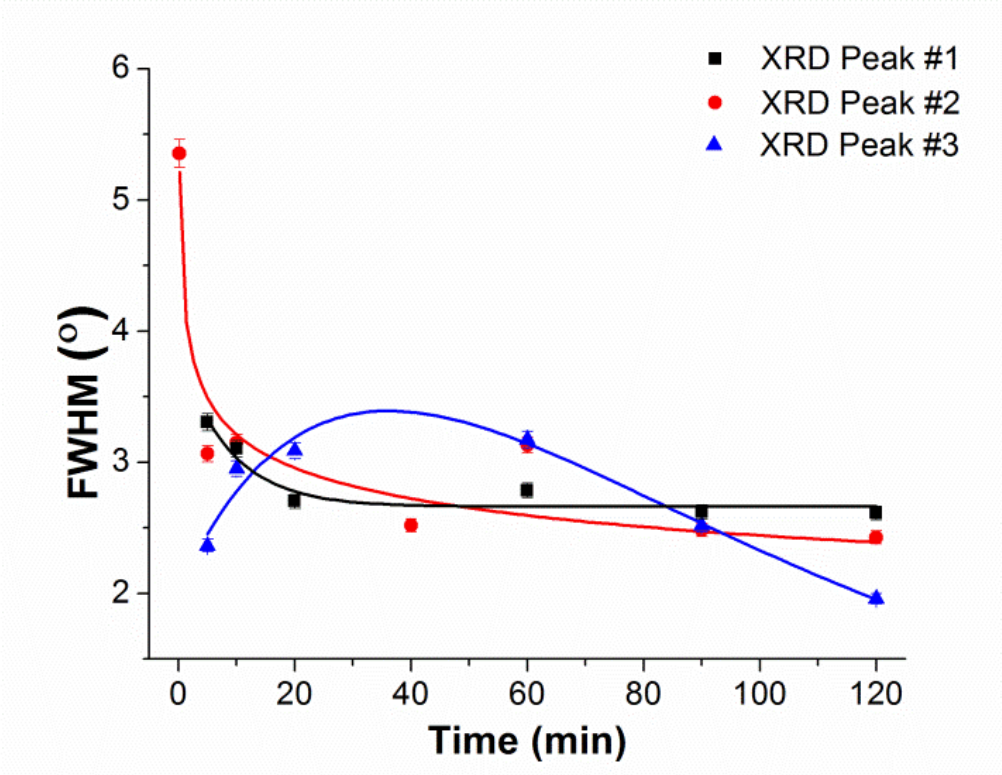

Figure 3.5 Comparison of fwhm measurements with growth time of the 3 primary diffraction peaks: peak #1 (1 1 1) [■], peak #2 (2 0 0) [●] and peak #3 (3 1 1) [▲].[58]

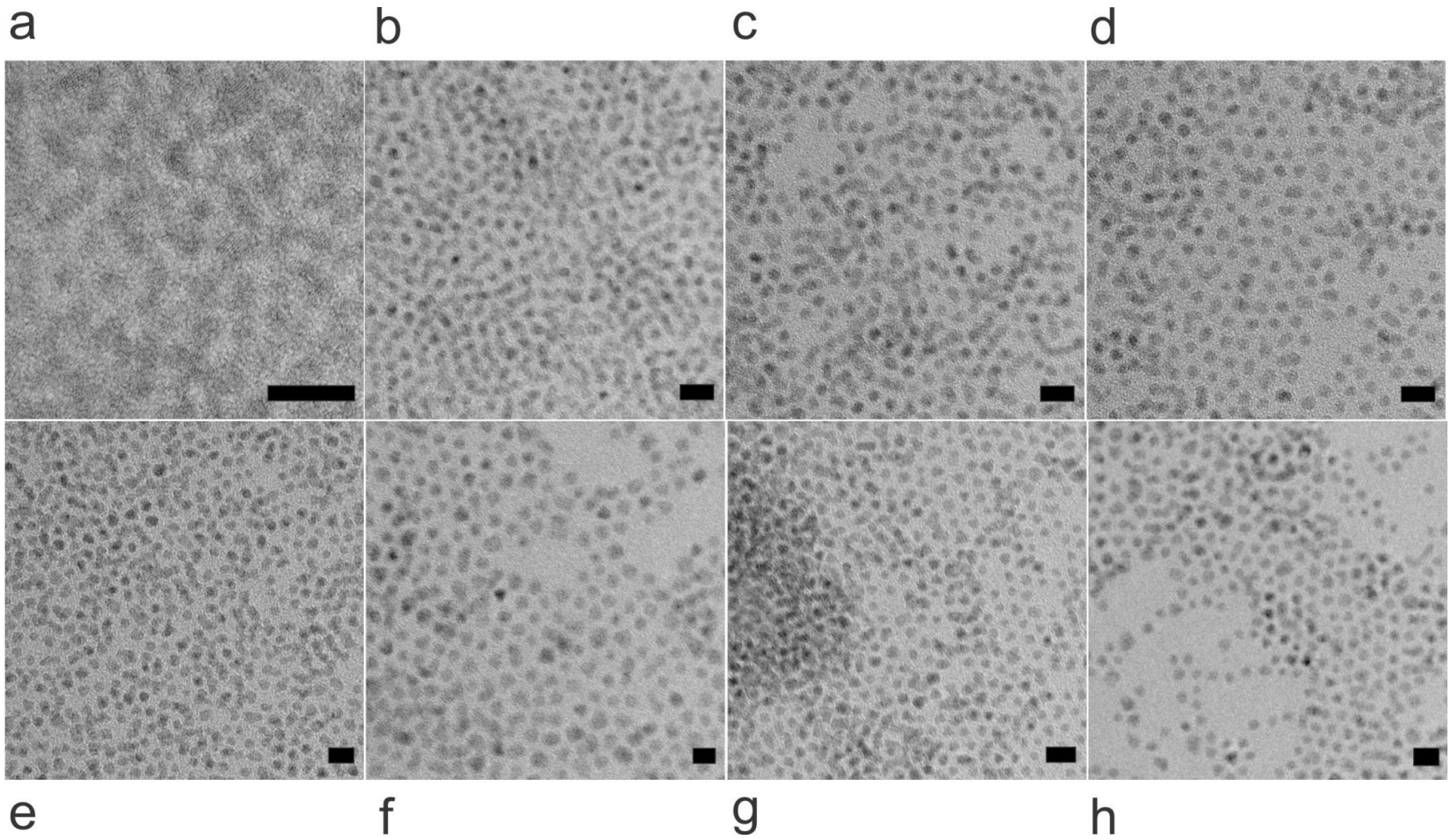

Figure 3.6 High resolution transmission electron micrographs of CdSSe nanocrystals with a chemical composition gradient, grown at T = 220°C with the following growth times: (a) 10 s, (b) 5 min, (c) 10 min, (d) 20 min, I 40 min, (f) 60 min, (g) 90 min and (h) 120 min, with size distributions in the range of 11.25% - 14.50%. All scale bars represent 10 nanometers in length.

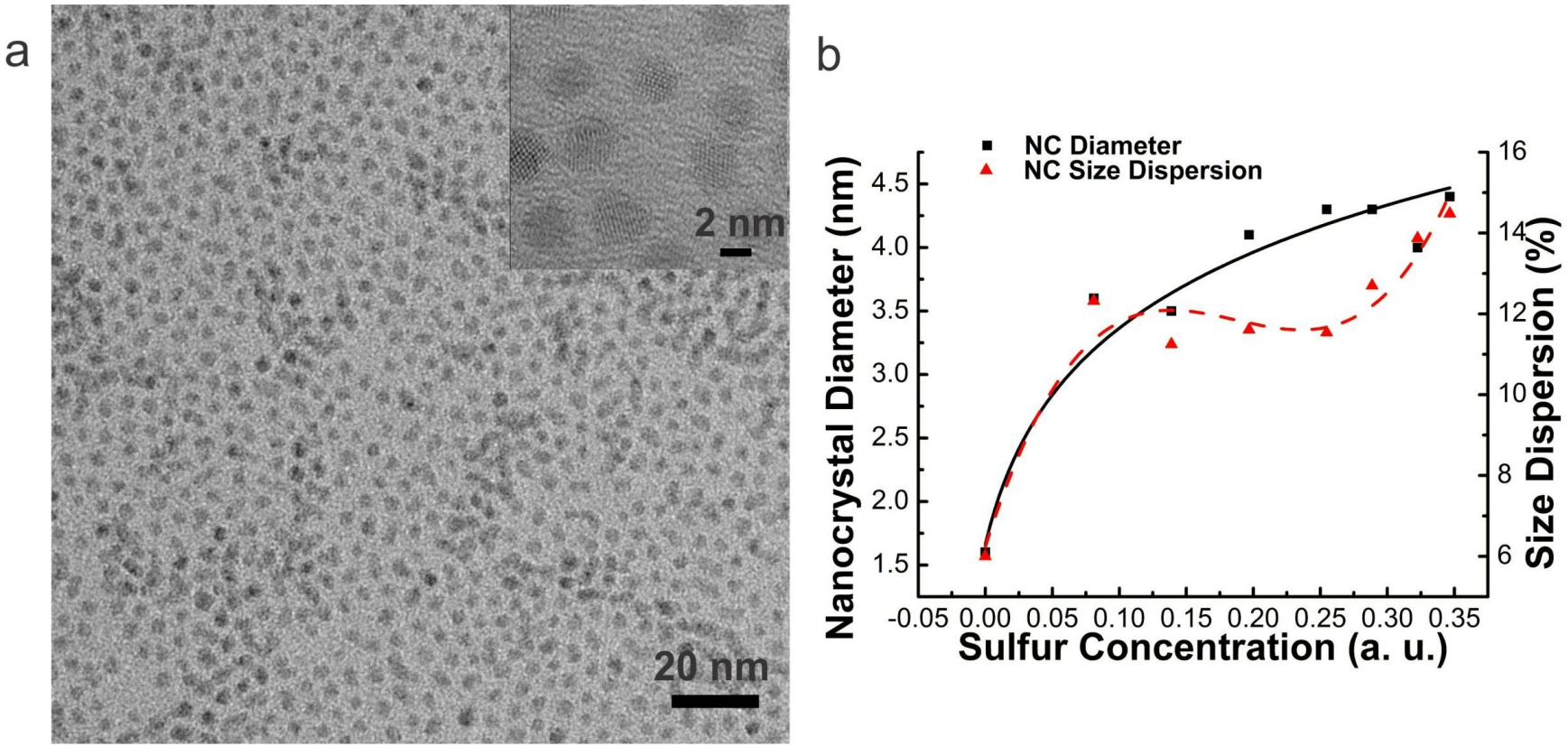

Figure 3.7 (a) High resolution transmission electron micrograph of ashperical CdSSe nanocrystals with a chemical composition gradient, grown at T = 220°C with a growth time of 120 min. Nanocrystals are approximately 4.4 nm in diameter with a size distribution of 14.50%. (b) Graph representing nanocrystal diameters [■] with increasing sulfur concentrations and the corresponding size distributions [▲].[58]

3.22.3 ***Photophysical Properties***

Absorption spectra obtained for the compositionally graded CdSSe nanocrystals with growth time are shown in Figure 3.8. The spectral shape and first absorption peak of the absorption spectrum for the 10 s sample, taken almost immediately after injection, is consistent with that of ultrasmall CdSe nanocrystals.[14b, c] This supports the idea that the growth of compositionally graded CdSSe nanocrystals progresses from CdSe nuclei.[72,73] As growth continues, the CdSSe nanocrystals exhibit red-shifted absorption, which eventually becomes stagnant prior to the termination of the synthesis. Though we observed changing S:Se ratios with growth time, analysis of the absorption spectra with growth time suggest that the compositionally graded CdSSe nanocrystals stop growing prior to terminating the reaction at 120 min.

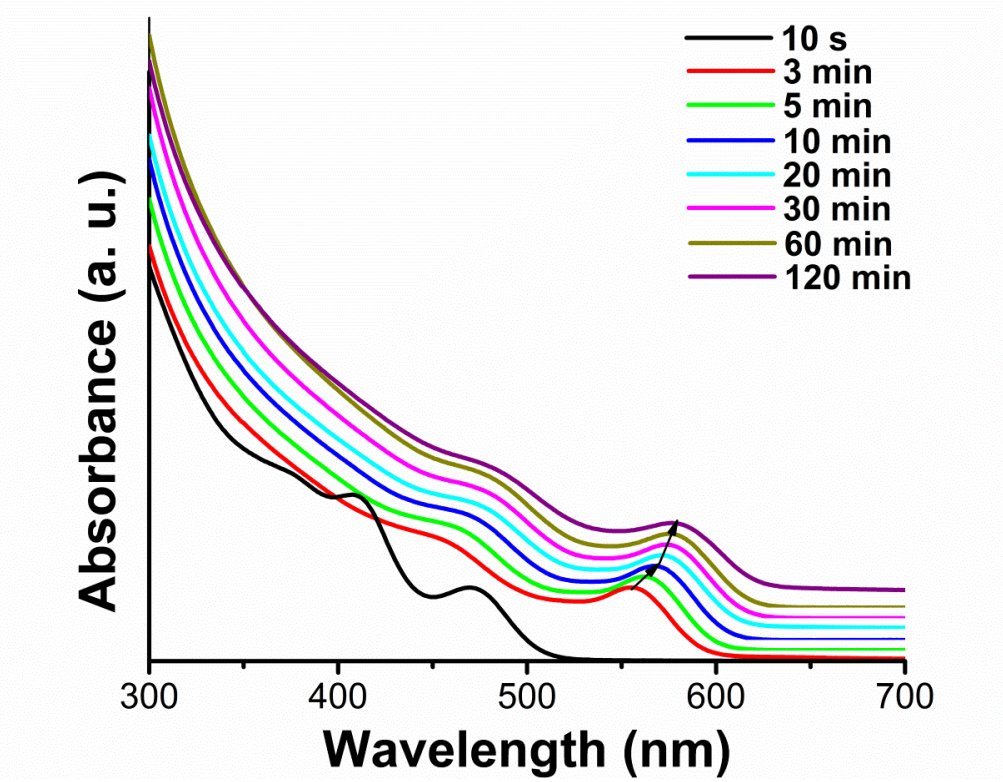

Figure 3.8 (a) Absorption spectra of CdSSe compositionally graded nanocrystal samples taken periodically during growth.

Alloys often exhibit optical properties that vary nonlinearly and are described by the following quadratic approximation (equation 3.1):

$$E_g(CdS_xSe_{1-x}) = xE_g(CdS) + (1-x)E_g(CdSe) - bx(1-x) \quad (3.1)$$

where b is the bowing parameter[74,75] and describes the degree of nonlinearity. The following equation corrects for the influence of structural confinement on the optical properties of alloy nanocrystals.

$$E_g = x\left[E_g(CdS,\infty) + \frac{a_1}{d} + \frac{c_1}{d^2}\right] + (1-x)\left[E_g(CdSe,\infty) + \frac{a_2}{d} + \frac{c_2}{d^2}\right] - b(d)x(1-x)$$

(3.2)

where d is nanocrystal diameter and a and c are empirical fit parameters. Nonlinearity observed in the optical properties of alloys are associated with the following factors: (1) distorted lattice constants, (2) deformation of electron distribution due to the differences in electronegativity of constituent atoms, and (3) variations in anion – cation bond lengths. The case of compositionally graded CdSSe is a bit more complicated.[74-75]

Band gap as a function of composition is plotted in Figure 3.9 and compared to band gap approximations for bulk and nanocrystal alloys using equations 3.1 and 3.2. Values for bowing parameter and the empirical fit parameters for the approximations were taken from the work of Swafford *et al*.[51] A quadratic fit is obtained for band gap as a function of time. The relationship is found in equation 3.3[58],

$$E_g = x\left[E_g(CdS,\infty) + A\right] + (1-x)\left[E_g(CdSe,\infty) + C\right] - bx(1-x) \quad (3.3)$$

where A and C are empirical fit parameters which have numerical values of -0.88 Ev and 0.53 Ev respectively. The bowing parameter for the compositionally graded CdSSe nanocrystals synthesized at T = 220°C is 1.09. Considering the optical properties of

gradient nanocrystals are not as strongly dependent on particle size as with homogeneous alloys, the relationship described in equation 3.3 is void a size parameter.

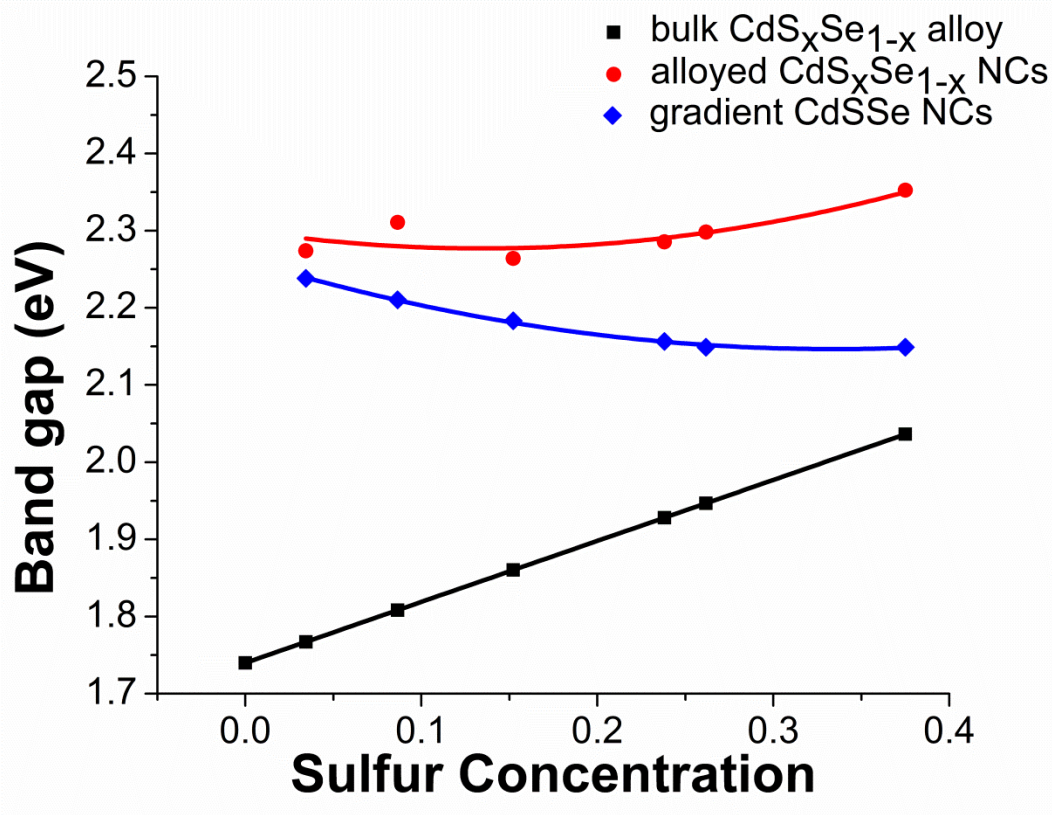

Figure 3.9 Band gap as a function of composition [♦] of compositionally graded CdSSe nanocrystals compared to band gap approximations for bulk semiconductor alloys [■] and semiconductor alloy nanocrystals [●].[58]

The departure of electronic structure of the compositionally graded CdSSe nanocrystals from the quadratic relationship presented for homogeneously alloyed semiconductor nanocrystals in equation 3.2 is depicted in Figure 3.10[51]. As shown in Figure 3.10, the correlation between particle size and band gap does not fit the approximation for homogenous alloys of CdS_xSe_{1-x}. Nonlinearities in the electronic

structure and optical properties of CdSSe nanocrystals are due to radially varying compositions which would produce non-uniformities in electron distributions, distortions in lattice constants and anion – cation bond lengths. Due to the heavier concentration of the more electronegative sulfur atoms towards the surface of the nanocrystal, we would expect higher concentrations of carriers in surface regions of the compositionally graded nanocrystals.

Distortions of lattice constants occur with the gradual introduction of sulfur as well. Sulfur has a smaller ionic radius than selenium, which would cause compressive strain on the crystal lattice of CdSSe with radial increases in length. In addition, anion – cation bond lengths would vary radially. These parameters facilitate widening of band gaps with radial length, similar to type-I core/shell materials but different from the abrupt interface associated with a two-step synthesis where core and shell materials are synthesized successively. And similar to core/shell materials, spatial confinement of carriers is primarily due to the spatial distribution of charges[39]. In the case of compositionally graded CdSSe nanocrystals, nanocrystal size has minimal effect on observed optical properties. Optical characteristics of these materials are governed by chemical composition gradients.

Aliquots taken immediately after injection demonstrate broad, white-light emissions shown in the inset of Figure 3.11a with a Stokes shift of 87 meV from the blue peak. This suggests that the growth of compositionally graded CdSSe progresses from ultrasmall CdSe nanocrystal cores. Bowers *et al* observed white light emissions from CdSe nanocrystals due to the extreme ratio of surface atoms to core atoms.[14c] Also in Figure 3.11a, PL spectra for compositionally graded CdSSe are shown with growth time.

Photoluminescence spectra are characterized by single, narrow peaks void of emissions associated with surface trap states or charging[76]. Figure 3.11b illustrates the narrow aspect of PL emissions from compositionally graded CdSSe. Although the size distribution of these nanocrystals broadens with growth time, the narrow emission observed in the PL of compositionally graded nanocrystals demonstrates uniformity in the optical properties. Size dispersions have negligible effect on the resultant optical properties of the gradient nanocrystals. Stokes' shifts for the gradient CdSSe nanocrystals were in the range of 38 meV – 54 meV. Absorption and PLE spectra of gradient alloys grown for 2 hours are shown in Figure 3.12.

A progressive change in spectral shape is also observed with increased growth time and increasing S concentrations. These changes are associated with peak broadening. Emission spectra for CdSSe compositionally graded nanocrystals grown for 1 hr, 1.5 hrs and 2 hrs, along with corresponding deconvolved spectra, are presented in Figure 3.13. Typically, with binary semiconductor nanocrystals or homogeneous alloyed nanocrystals, peak broadening would also be associated with a polydispersion in nanocrystal size. Governing quantum confinement effects would be dramatically dependent on crystal diameter and the resultant PL spectrum would be a convolution of emissions from nanocrystals luminescing at different wavelengths. Previous discussions on the absorption and photoluminescence of these materials have described the optical properties of the CdSSe gradient nanocrystals as being independent of particle size. An increase in particle size of gradient CdSSe has a negligible effect on the resultant optical properties. Instead, the optical properties of gradient CdSSe nanocrystals are governed

by their radially dependent crystal arrangement. Variations in spectral shape observed in the emission of gradient CdSSe nanocrystals are not due to broadening size dispersions. It can also be argued that with increased growth times, nucleation and growth of binary CdS occurs and observed photoluminescence spectra are convolutions of emitting CdSSe nanocrystals and CdS nanocrystals. This hypothesis is somewhat supported by the emergence of the (2 2 0) diffraction peak of CdS in XRD spectra (Figure 3.3b) with increased growth times. However, the bulk band gap energy for CdS is 2.53 Ev[77] (or 491 nm) which, with quantum confinement effects, would result in the CdS nanocrystal luminescing at larger energies and shorter wavelengths than what is reported.

We have not yet developed a working theory to describe the emergence of the surplus photoluminescence peaks. This phenomenon was initially thought to be due to biexciton emission. Biexcitons have been observed due to the following occurences: 1) excitation from a single-exciton band to the biexciton band, 2) two-photon absorption of light from the ground state to the biexciton state and 3) luminescence from a biexciton state from two free excitons in a dense exciton state[78]. Semiconductor nanocrystals with chemical composition gradients are described by having a smooth potential energy diagram which depicts a progression from discrete energy levels[48, 50, 55], typical of binary semiconductor nanocrystals, homogeneously alloyed nanocrystals and core/shell particles. Valence and conduction bands are likely to consist of more closely spaced energy levels as opposed to being continuous, as in bulk materials. Once forbidden transitions are now made available due to gradually changing chemical composition and crystal structure which could allow for at least three possible outcomes: 1) monochromatic photoexcitation of the gradient nanocrystals promotes electrons to the

same excited state, followed by relaxation to different yet closely spaced energy levels prior to emission, resulting in multi-wavelength emissions; or 2) photon absorption in gradient nanocrystals promotes electrons to different, yet closely spaced , excited states followed by relaxation and emission of photons with varying energies; or 3) a combination of both 1 and 2. Each proposed outcome is possible with two-photon absorption. Wang *et al*. observed tri-peak emissions thought to be due to the presence of trions as a result of the induced composition gradient[55]. An experiment probing the photoluminescence of a single particle could prove or disprove this theory.

Quantum yield (QY) values with growth time are plotted in Figure 3.14. Values up to 67% are reported here for Qys of compositionally graded CdSSe nanocrystals with 1:1 S to Se precursor ratios. Radial variances in composition and lattice constants in CdSSe nanocrystals produce increased values of QY with increasing growth times. Higher concentrations of sulfur atoms toward the surface of CdSSe nanocrystals results in carrier confinement towards the core, similar to type-I core/shell nanocrystals, and increased emission intensities[39]. Enhancements in QY may also be due to reduced non-radiative processes and increased radiative transitions as a result of the compositionally graded structure configuration[48]. Images of UV-illuminated samples of compositionally graded CdSSe are shown in Figures 3.14a-c to demonstrate the observable change in intensity with growth time. Figure 3.14c is a monochromatic image of the UV-illuminated sample which is intended to demonstrate the intensity of emissions.

Optical characteristics of these materials are governed by chemical composition gradients which are directly related to the resultant spatial charge distributions.[55] We propose a phenomenon in which carriers are confined at some depth below the surface of

the nanocrystal by an energy barrier resulting from increasing concentrations of charge moving radially outward. The depth of confinement is directly related to the radial variances in structure and stoichiometry and its effect on the induced electron distribution of the nanocrystal. For this synthetic approach, the radially varying S: Se ratio is the result of disparate anionic precursor rate constants, k_1 and k_2.

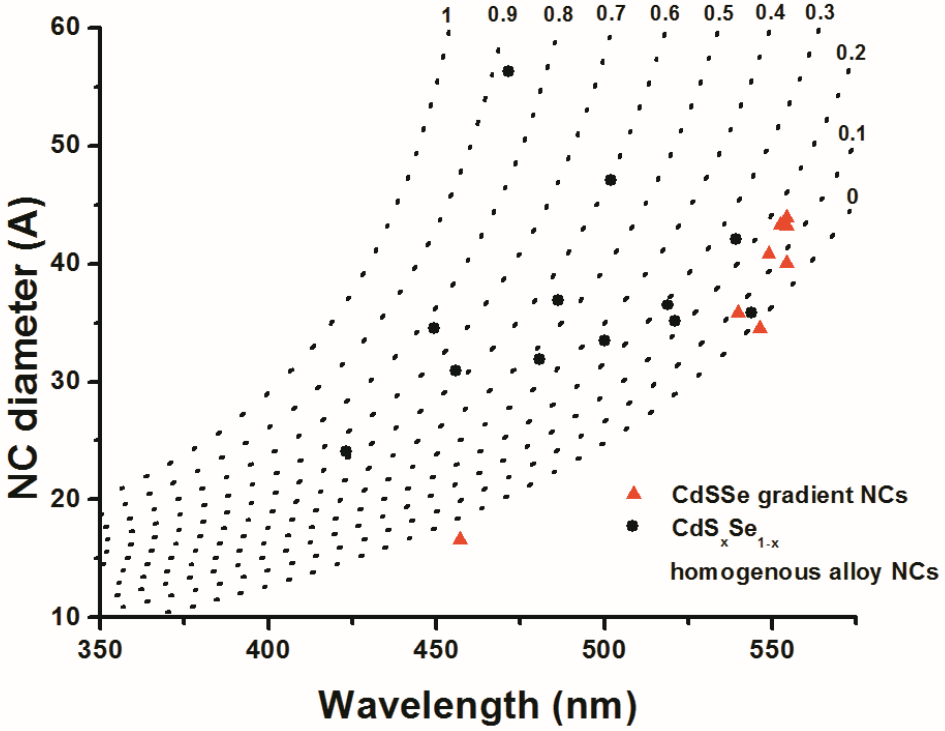

Figure 3.10 Graph representing values associated with the size-dependent, quadratic expression for band gap energy calculations for homogeneously alloyed CdS_xSe_{1-x} nanocrystals[51]. Data for both compositionally graded CdSSe [▲] and homogenously alloyed CdS_xSe_{1-x} [●] are compared to demonstrate the departure of the optical properties of compositionally graded CdSSe from this approximation.

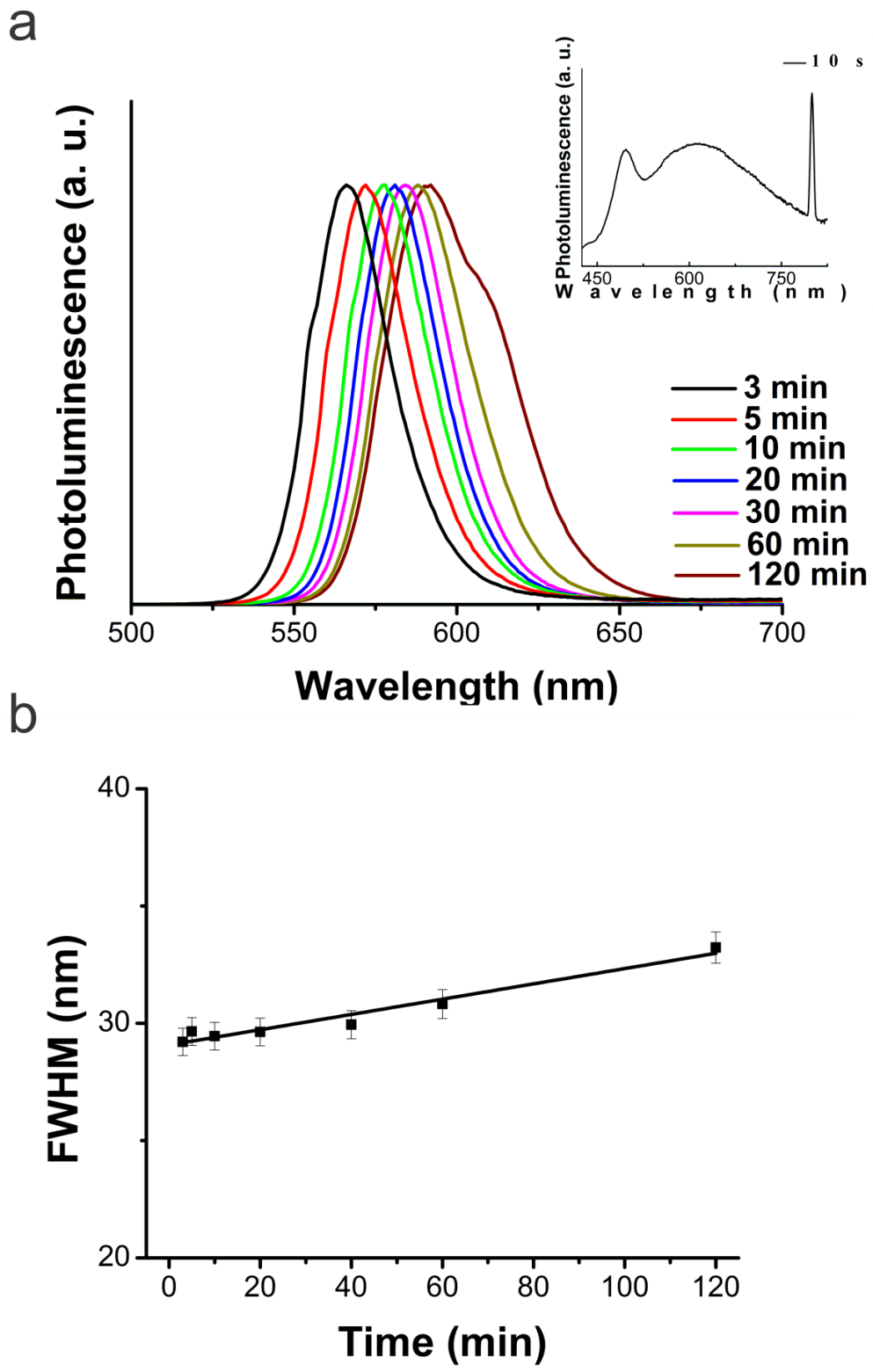

Figure 3.11 (a) Normalized PL spectra of compositionally graded CdSSe nanocrystals with growth time. Inset: PL of aliquot taken immediately after injection and exhibiting broad emissions. (b) Full width at half maximum (FWHM) values of PL peaks plotted versus growth time.[58]

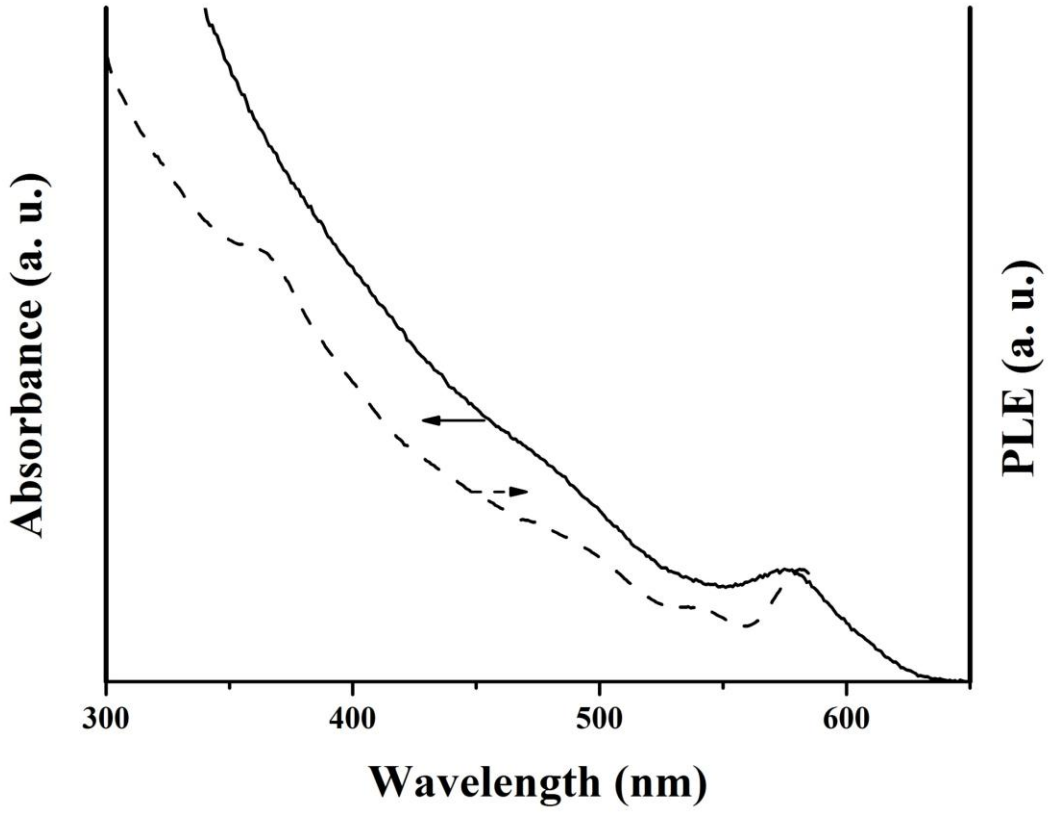

Figure 3.12 Absorption (solid line) and PLE (broken line) spectra of gradient CdSSe nanocrystals grown for 2 hrs.

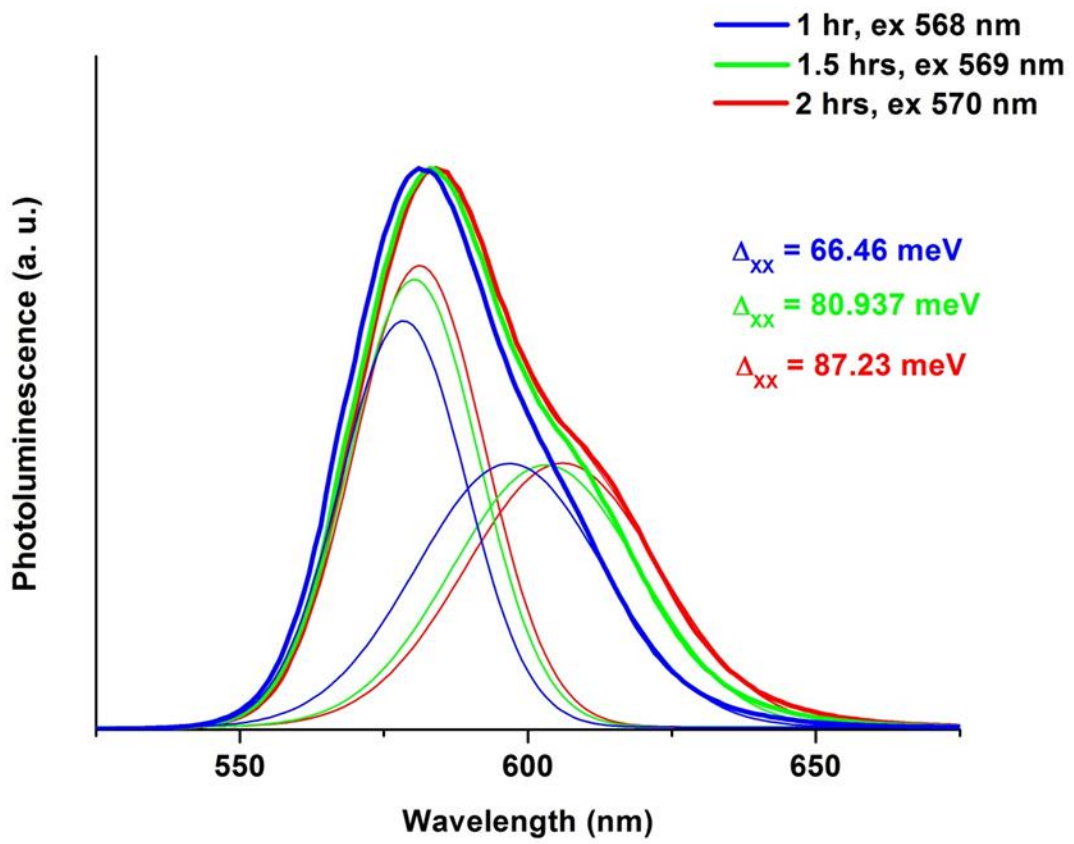

Figure 3.13 Deconvoluted, asymmetrical PL peaks of CdSSe (T = 220°C) grown for 1 hr, 1.5 hrs and 2 hrs. Δ_{XX} describes the distance between the two deconvoluted peaks associated with the photoluminescence spectrum for each growth time.

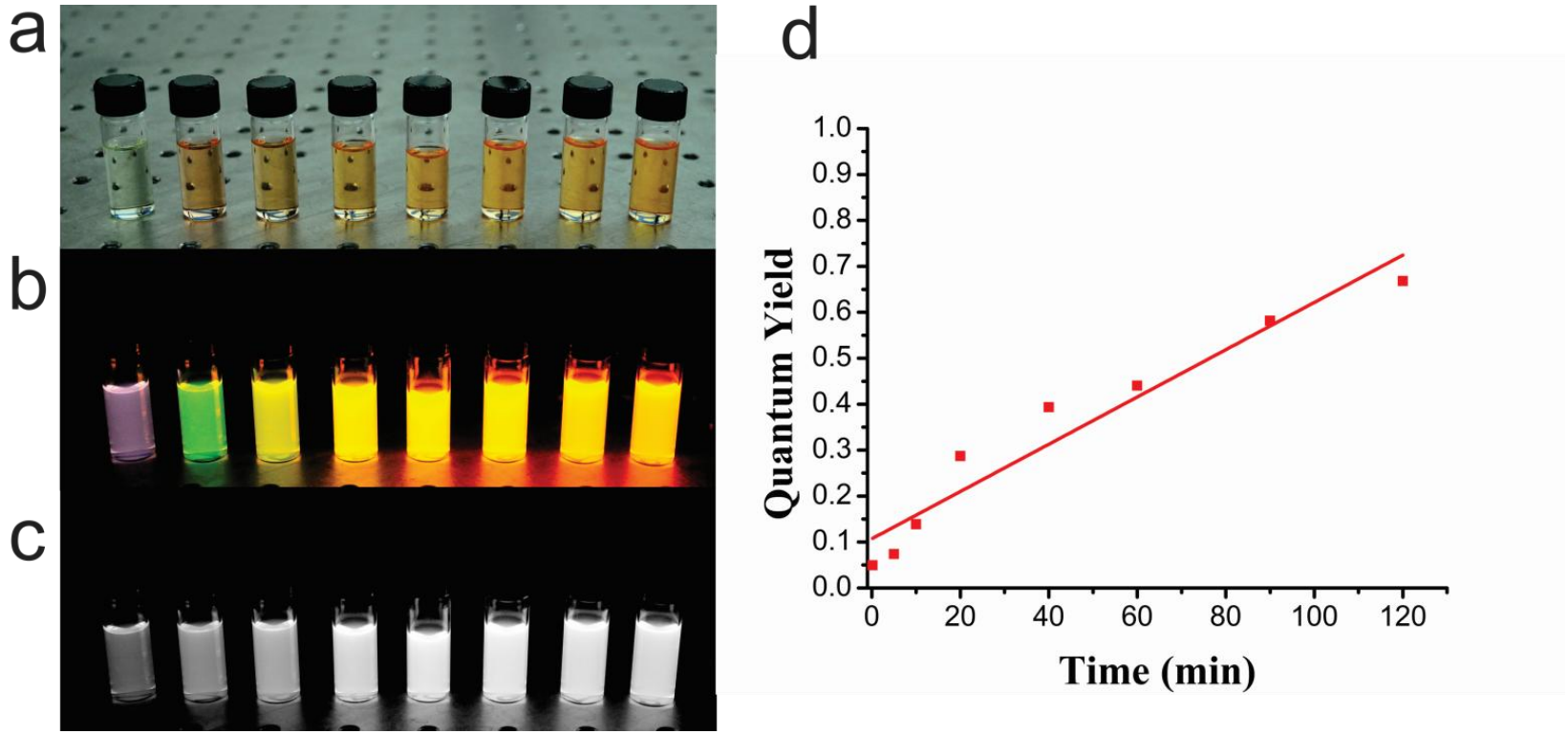

Figure 3.14 Photographs of CdSSe nanocrystals with a chemical composition gradient (a) under ambient light, (b) with UV illumination and (c) a monochromatic image of UV illuminated nanocrystals with increasing growth time from left to right. (d) Quantum yield as a function of growth time.[58]

3.23 **Temperature Dependent Gradation**

To further elucidate the effects of the degree of gradation on the optical characteristics, additional syntheses were carried out at the following temperatures: 150°C, 240°C, 260°C and 315°C. Considering the relationship between reaction rate and temperature described in equation 2.2, we anticipated variances in precursor reaction rates with changing synthesis temperatures. Elevated temperatures facilitated more rapid reaction rates of both S:TBP and Se:TBP precursors, altering resultant anionic stoichiometries. Figure 3.15 shows the variations in sulfur concentration of the gradient nanocrystals with growth time and due to modified synthesis temperatures.

The S:TBP precursors were not activated during synthesis at T = 150°C and produced nanocrystals void of sulfur. From this point forward, the discussion will be restricted to ternary materials produced by these syntheses. Once S precursors are activated in the T = 315°C syntheses, anionic ratios remain fairly constant with increasing growth times, similar to that of homogeneous alloys. At reaction temperatures of 220°C, 240°C and 260°C, sulfur concentrations vary with growth time, indicating the formation of nanocrystals with chemical composition gradients. A correlation between the progressions of stoichiometries as a function of temperature cannot be established with this experimental data. TEM images of CdSSe nanocrystal samples grown at T = 240°C, T = 260°C and T = 315°C are shown in Figures 3.16 – 3.18.

Optical characteristics of the CdSSe nanocrystals synthesized at varying temperatures are depicted in Figure 3.19. Here, we compare the progression of the first absorption peak with growth time at varying synthesis temperatures. Absorption wavelengths fluctuate with changing temperatures but appear to show no trend as a function of temperature. Progressions of the absorption spectra with growth time follow

similar trends even with dramatic differences in gradation. This data supports the proposed phenomenon of carrier confinement, where unchanged absorption with changing composition is observed. Band edge absorptions as a function of anionic stoichiometries were fit to equation 3.3 to determine bowing parameters for gradient CdSSe nanocrystals produced at each synthesis temperature (Figure 3.20). Resultant parameters are summarized in Table 1 and empirical fits for the ternary gradient nanocrystals are as follows:

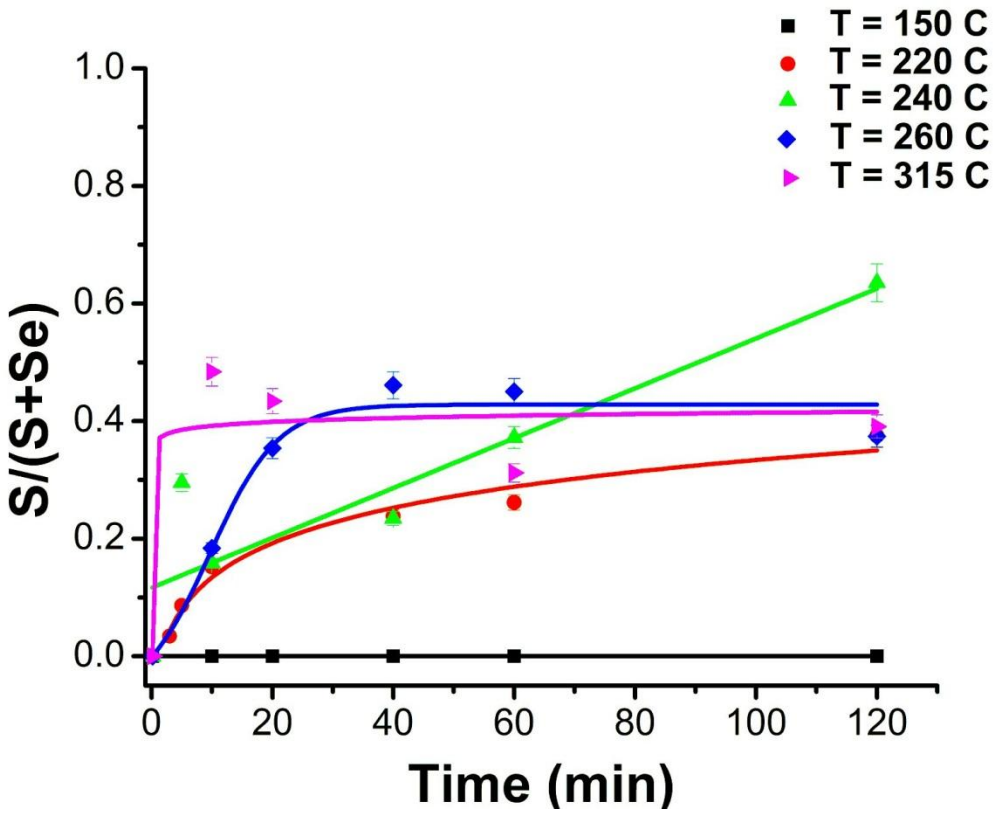

Figure 3.15 Stoichiometric data of compositionally graded CdSSe nanocrystals demonstrating progressions of sulfur concentrations with growth time and per temperature; 220°C [●], 240°C [▲], 260°C [♦] and 315°C [►]. Data obtained from RBS measurements.[58]

for T = 220°C:

$$E_g = x\left[E_g(CdS,\infty) - 0.88\right] + (1-x)\left[E_g(CdSe,\infty) + 0.53\right] - 1.09x(1-x) \qquad (3.4)$$

for T = 240°C:

$$E_g = x\left[E_g(CdS,\infty) - 0.88\right] + (1-x)\left[E_g(CdSe,\infty) + 0.45\right] - 0.28x(1-x) \qquad (3.5)$$

for T = 260°C:

$$E_g = x\left[E_g(CdS,\infty) - 1.27\right] + (1-x)\left[E_g(CdSe,\infty) + 0.47\right] - 4.87x(1-x) \qquad (3.6)$$

for T = 315°C:

$$E_g = x\left[E_g(CdS,\infty) + 2.44\right] + (1-x)\left[E_g(CdSe,\infty) + 0.65\right] - 1.29x(1-x) \qquad (3.7)$$

Tables 2-5 contain experimental data used to obtain empirical fits. Emission wavelengths as a function of sulfur concentration at varying temperatures are plotted in Figure 3.21a. Slightly red-shifted emissions are observed for syntheses at temperatures of 220°C and 240°C with increasing sulfur content; emission wavelengths, however, remain fairly consistent for nanocrystals synthesized at temperatures of 260°C and 315°C. Figure 3.21b depicts FWHM values of PL peaks for nanocrystals synthesized at different temperatures. Gradient nanocrystals demonstrated narrow emission with FWHM values ranging between 24.5 nm and 33 nm. Calculated quantum yields for CdSSe nanocrystals synthesized at various temperatures are presented in Figure 3.21c.

Compositionally graded CdSSe nanocrystals synthesized at T = 220°C produces emissions with the highest quantum yields of the materials discussed here. For that synthesis, quantum yields increase quadratically with growth time. This also demonstrates improvements from quantum yields of binary nanocrystals. Irregular quantum yield progressions may be the result of changing electronic structures of the

gradient nanocrystals with increasing sulfur stoichiometries and fluctuations due to the degrees of gradation which govern confinement effects.

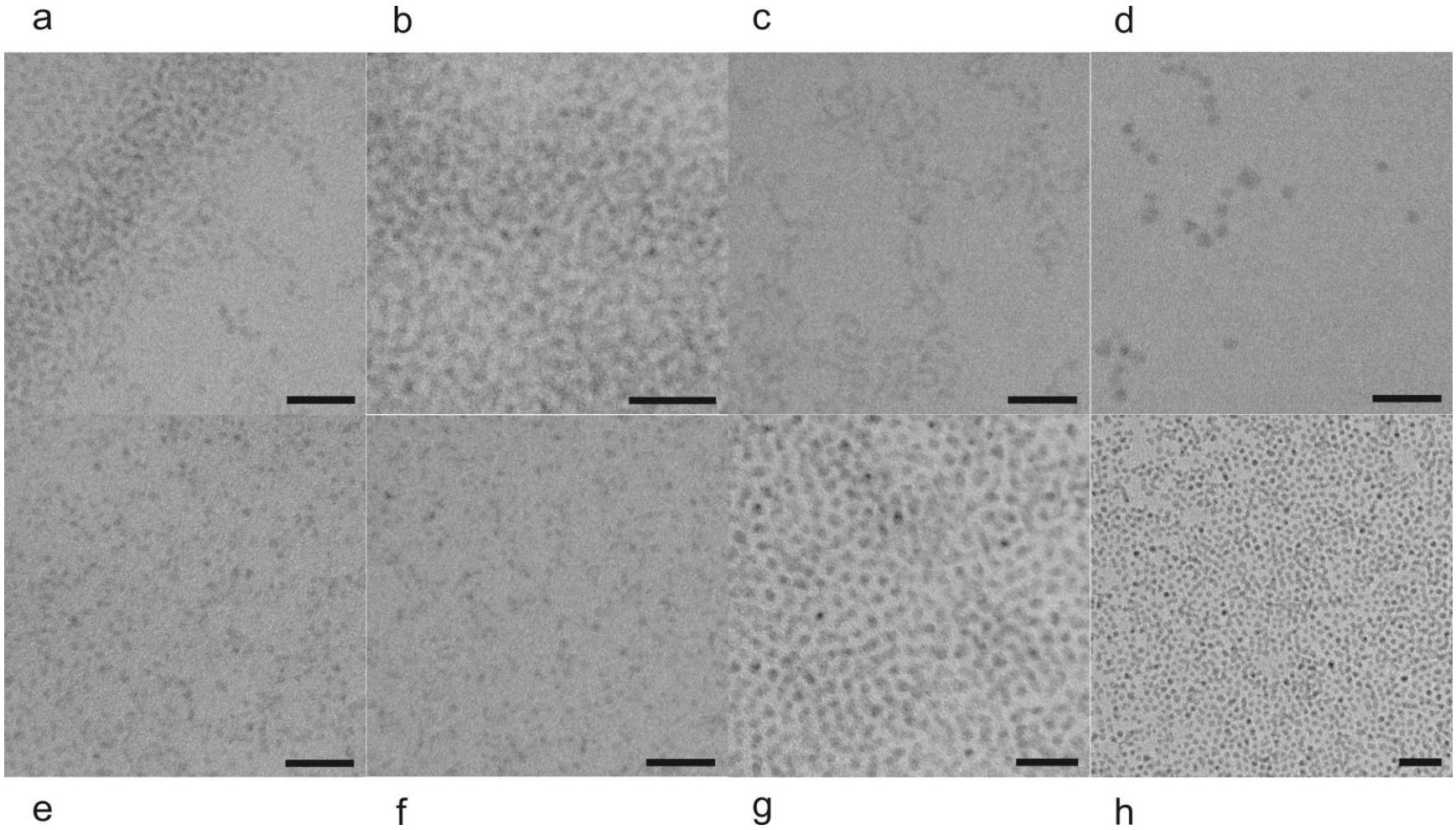

Figure 3.16 TEM micrographs of compositionally graded CdSSe nanocrystal synthesized at T = 240°C. Samples represent aliquots taken at the following times: (a) 10 s, (b) 5 min, (c) 10 min, (d) 20 min, I 40 min, (f) 60 min, (g) 90 min and (h) 120 min. All scale bars represent 20 nm.

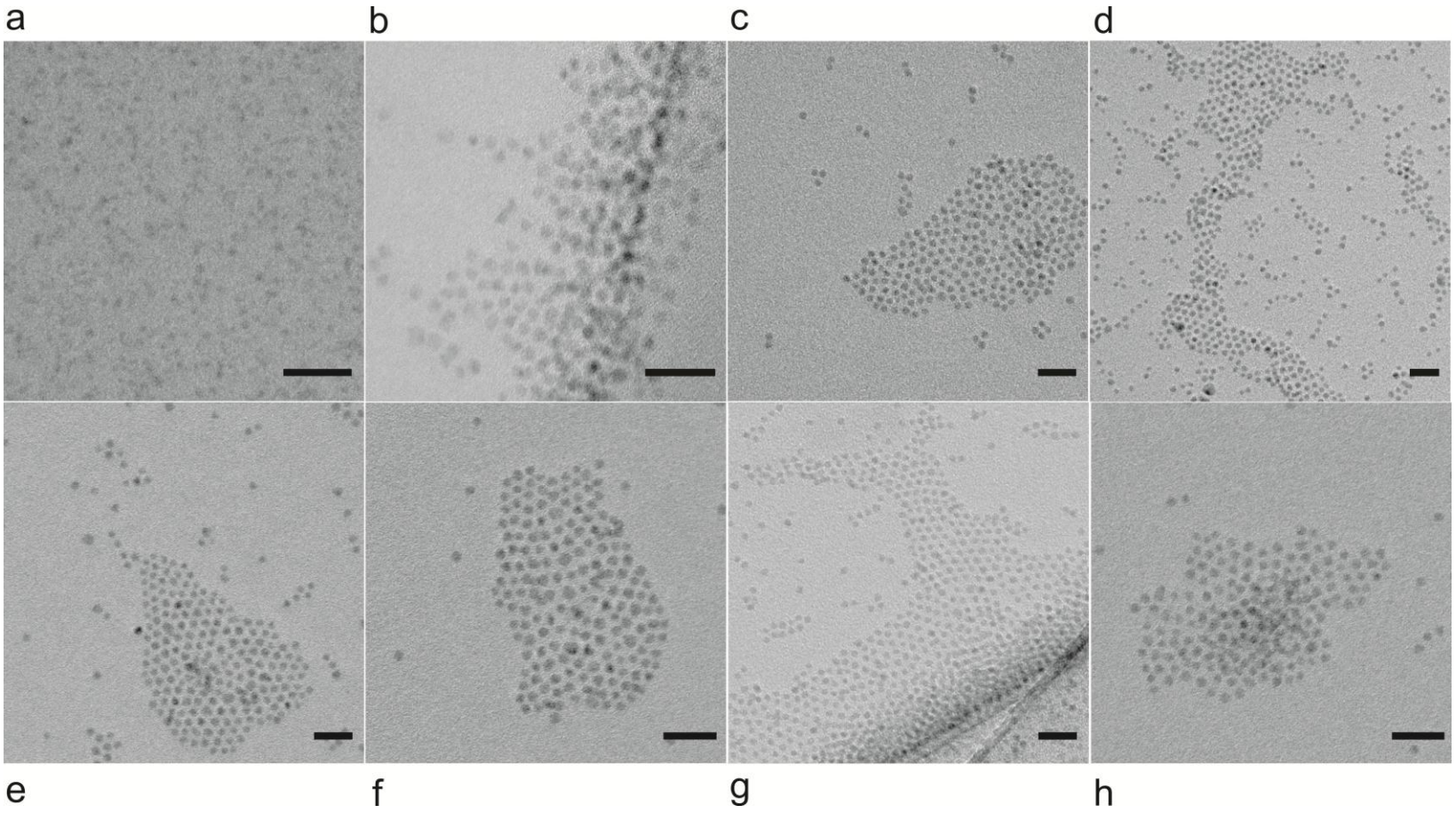

Figure 3.17 TEM micrographs of compositionally graded CdSSe nanocrystal synthesized at T = 260°C. Samples represent aliquots taken at the following times: (a) 10 s, (b) 5 min, (c) 10 min, (d) 20 min, I 40 min, (f) 60 min, (g) 90 min and (h) 120 min. All scale bars represent 20 nm.

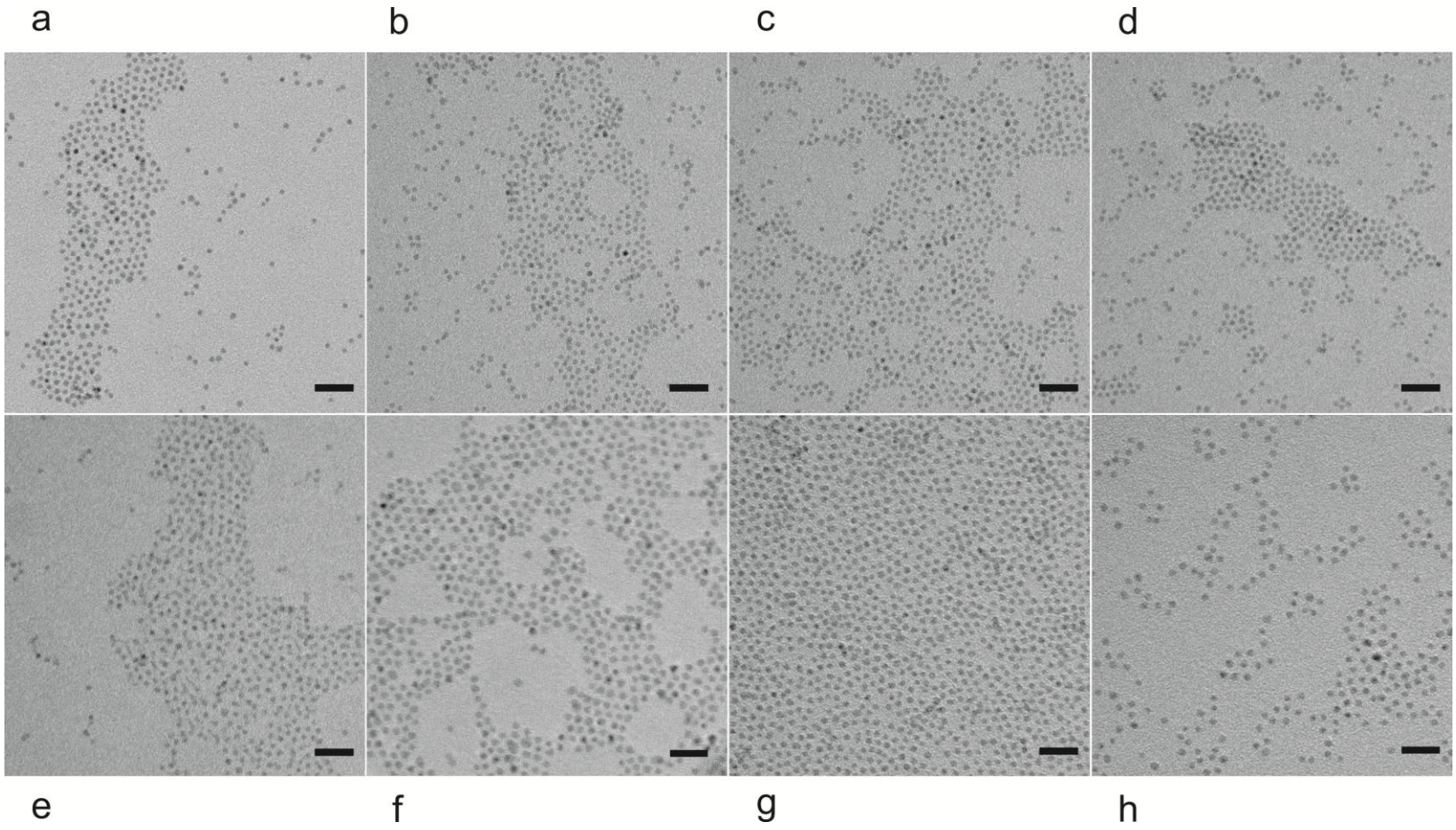

Figure 3.18 TEM micrographs of compositionally graded CdSSe nanocrystal synthesized at T = 315°C. Samples represent aliquots taken at the following times: (a) 10 s, (b) 5 min, (c) 10 min, (d) 20 min, I 40 min, (f) 60 min, (g) 90 min and (h) 120 min. All scale bars represent 20 nm.

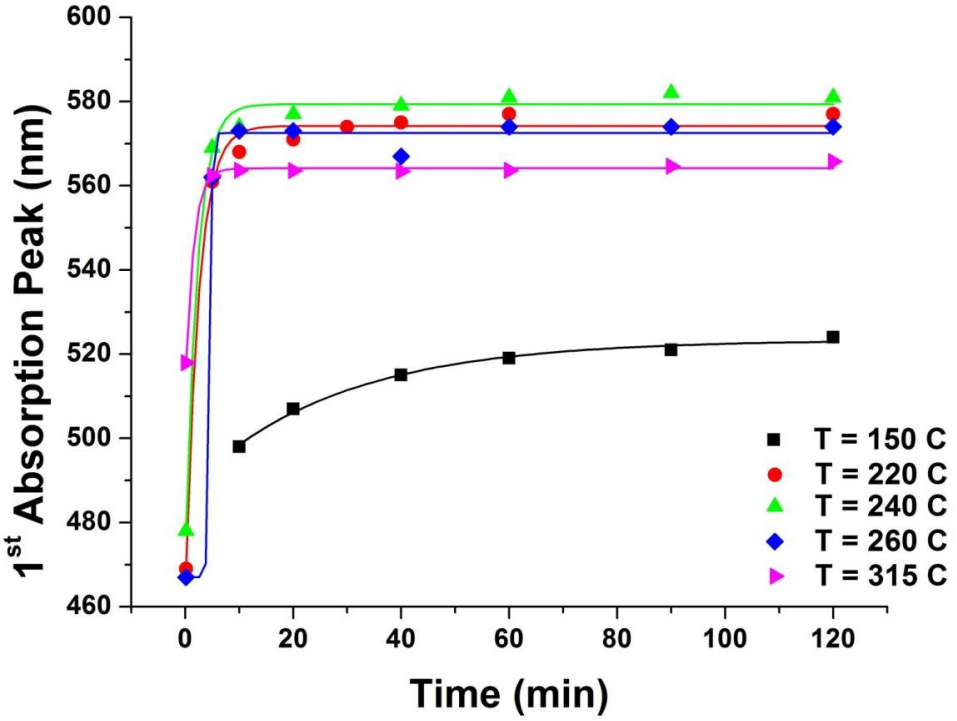

Figure 3.19 Comparisons of the (a) first absorption peak and (b) emission wavelength during growth and with varying temperatures; 220°C [●], 240°C [▲], 260°C [♦] and 315°C [►].[58]

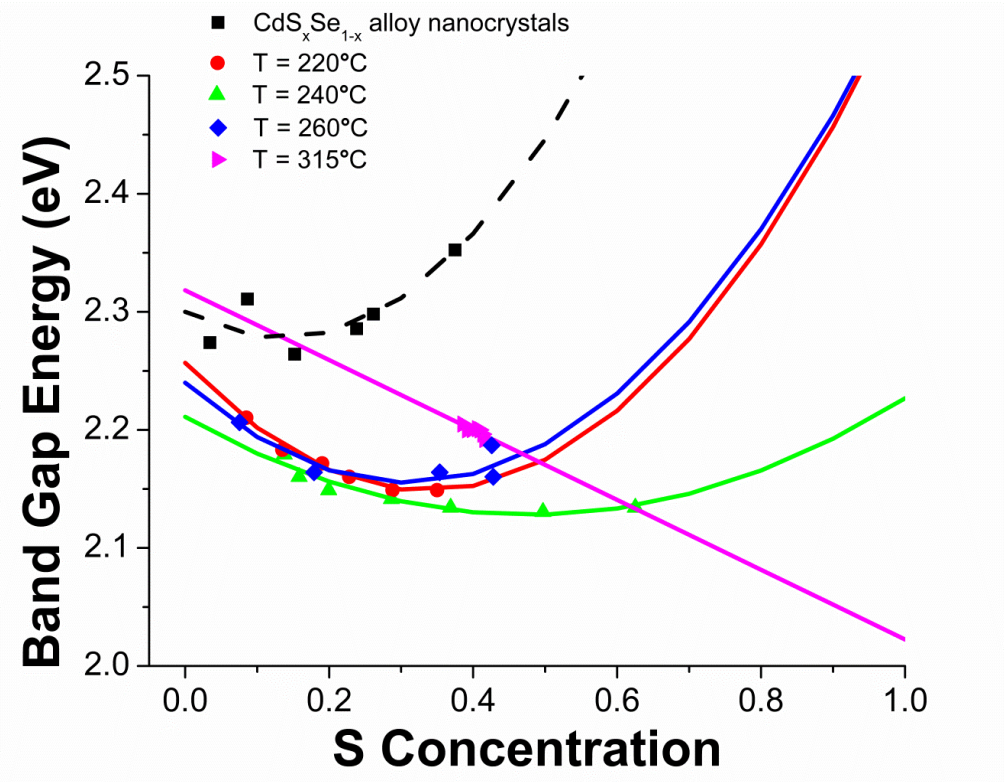

Figure 3.20 Compositionally graded CdSSe nanocrystals synthesized at varying temperatures, compared to homogeneously alloyed CdS_xSe_{1-x} nanocrystals[79] fit to Equation 3.3.[58]

Table 1. Fitting Parameters for Calculation of Bowing Constant

T (°C)	***A*** [a] (eV)	***C*** [a] (eV)	***B***
220	-0.88 ± 0.01	0.53 ± 0.06	1.09 ± 0.12
240	-0.88 ± 0.09	0.45 ± 0.02	0.28 ± 0.11
260	-1.27 ± 0.48	0.47 ± 0.05	4.87 ± 0.99
315	2.44 ± 0.05	0.65 ± 0.01	1.29 ± 0.10

[a]Fitting our data for band edge absorption as a function of anionic stoichiometries produces a quadratic approximation described in equation 3.3. A (CdS) and C (CdSe) are the corresponding empirical parameters.[58]

Table 2. T=220 C, Sulfur Concentrations and Band Gaps

S/(S+Se)	Band Gap (eV)
0.000	2.644
0.087	2.210
0.152	2.183
0.238	2.157
0.262	2.149
0.375	2.149

Table 3. T=240 C, Sulfur Concentrations and Band Gaps

S/(S+Se)	Band Gap (eV)
0.000	2.594
0.159	2.160
0.235	2.142
0.372	2.134
0.636	2.134

Table 4. T=260 C, Sulfur Concentrations and Band Gaps

S/(S+Se)	Band Gap (eV)
0.000	2.655
0.184	2.164
0.354	2.164
0.461	2.187
0.450	2.160
0.374	2.603

Table 5. T=315 C, Sulfur Concentrations and Band Gaps

S/(S+Se)	Band Gap (eV)
0.000	2.394
0.484	2.200
0.434	2.200
0.312	2.200
0.391	2.192

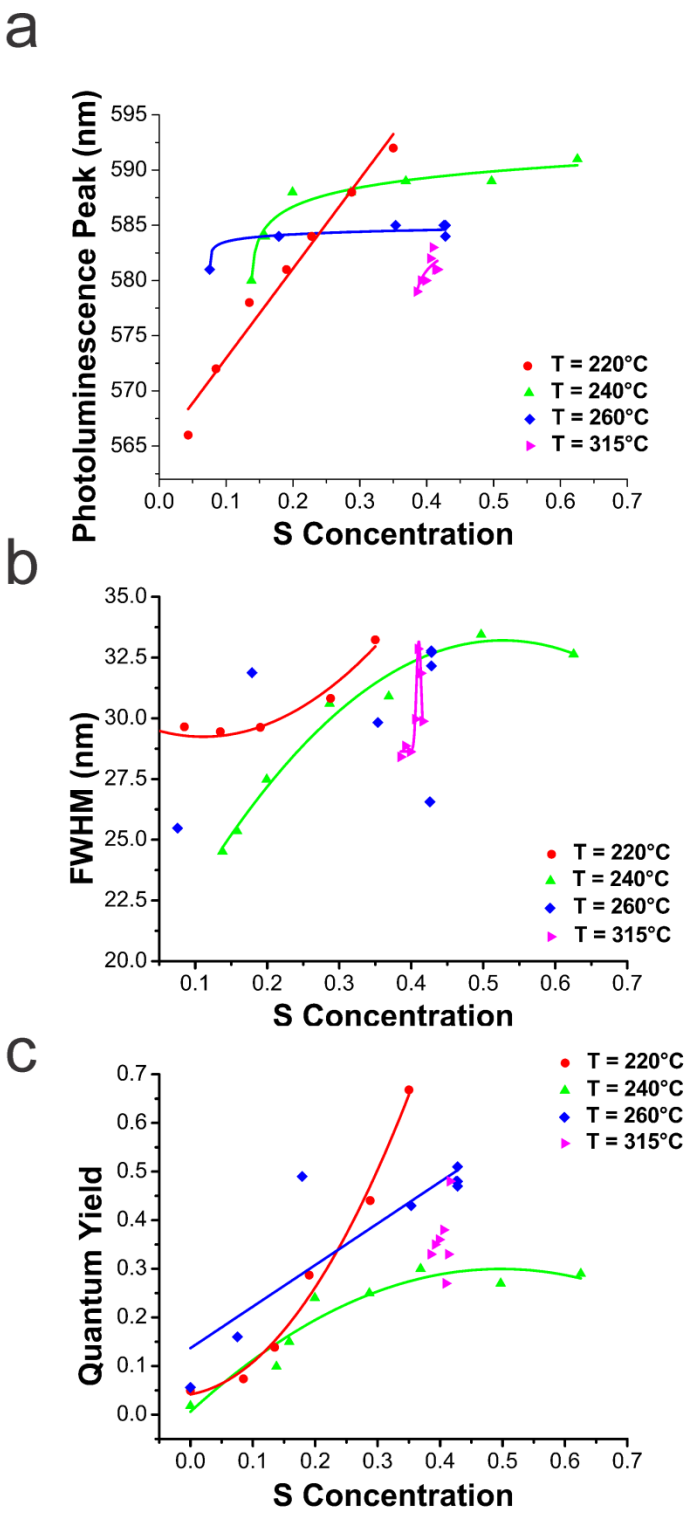

Figure 3.21 Here, we illustrate (a) photoluminescence as a function of sulfur concentration at 220°C [●], 240°C [▲], 260°C [♦] and 315°C [►]. Their corresponding (b) FWHM and (c) QY values as a function of sulfur concentration are also demonstrated.[58]

3.24 **Improved Luminescence Intensity with Changing Anionic Stoichiometries**

In an attempt to enhance the optical properties of the compositionally graded CdSSe nanocrystals, initial anionic precursors were varied. Considering that syntheses at T = 220°C produced gradient nanocrystals with the highest luminescence efficiencies, this reaction temperature was used. Figure 3.22a shows resultant absorption and emission wavelengths of compositionally graded CdSSe nanocrystals with varying anionic precursor ratios. In the analysis of both absorption and emission properties of the gradient CdSSe nanocrystals, negligible shifts are observed with changing anionic precursor concentrations. To complement these findings, FWHM values and Stokes shifts are plotted in Figure 3.22b with increasing Se concentrations. We mostly observe a linear change in luminescence efficiencies with increasing concentrations of S precursors and decreasing concentration of Se precursors; whereas compositionally graded CdSSe nanocrystals demonstrate higher quantum yields with higher concentrations of S precursors. This is evident in Figure 3.22c and the highest observed quantum yield was 74%.

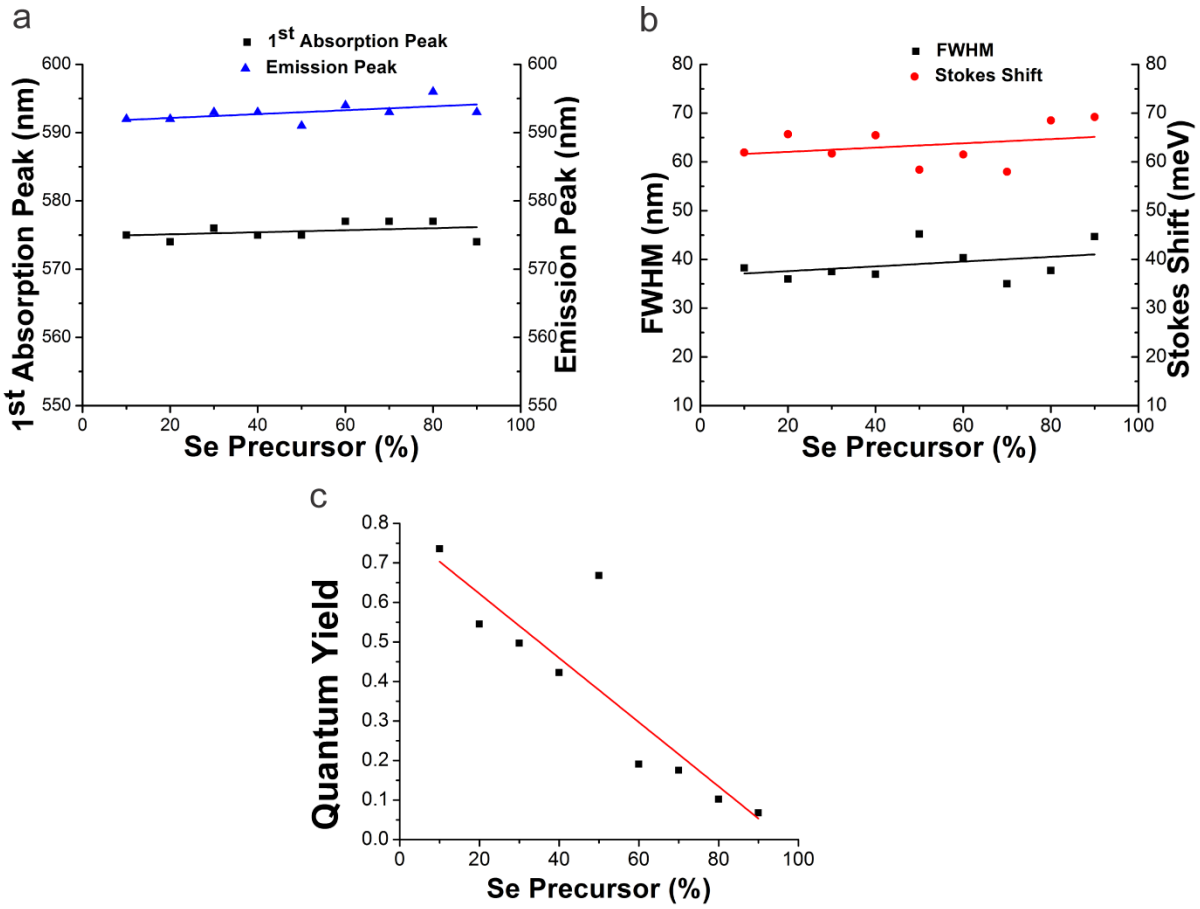

Figure 3.22 Comparisons of the (a) first absorption peaks, (b) FWHM values and Stokes Shifts, and (c) quantum yields of compositionally graded CdSSe nanocrystals synthesized at T = 220°C for 2 hours and fabricated with varying anionic precursor ratios. With increasing S precursor concentrations and decreasing Se precursor concentrations, negligible variation in absorption and emissions are observed, yet luminescence efficiencies increase.[58]

CHAPTER IV

CONCLUSIONS AND FUTURE DIRECTIONS

This dissertation explored the structural configuration and resultant optical properties of CdSSe nanocrystals exhibiting chemical composition gradients with varying degrees of gradation, produced by tuning anionic precursor reactivity via temperature.

A gradual incorporation of S atoms into the nanocrystal matrix was paired with stoichiometric analysis, where the anionic ratios were measured, with nanocrystal growth time. Structural analysis also reveals slight deviations in the crystalline structure of gradient CdSSe nanoparticles compared to bulk CdSe and CdS crystals. Considering the difference in anionic diameters, where Se has a larger ionic radius compared to S, distortions in crystal structure were anticipated with increasing S concentrations. The resultant crystal is severely strained, in which the zinc blende crystal structure is continued throughout the nanoparticle but the unit cell building blocks are incorporated with non-uniform distortions. We propose that growth of the compositionally graded CdSSe nanocrystals initiates from ultra-small CdSe nanocrystals and continues with the gradual incorporation of S atoms creating a radially-directed, chemical composition gradient. It is also possible that gradient CdSSe nanocrystals are formed by the gradual diffusion of S atoms into CdSe nanocrystals. If this has occurred, the configuration would closely resemble a core/shell particle. Based on stoichiometric data and structural analysis, we are only able to simply determine that binary CdSe nanocrystals are present at the beginning of the synthesis and S concentrations increase with growth time.

Though the latter growth mechanism is possible, our data supports the former conjecture for growth.

Similar to a multilayered particle, gradient nanocrystals are composed of layered materials each having its own electronic structure. The gradation allows for smoothened transitions between layers and also describes the internal crystal structure and defines the resultant quantum confinement effects. Carriers are confined at some depth below the surface of the nanocrystal by an energy barrier associated with increasing concentrations of charge towards the nanocrystal surface. The depth of confinement is independent of nanocrystal diameter but varies according to gradation. Induced disparities in composition gradation allow for tunability of electronic structures of these materials by merely manipulating rate constants of precursors. The combination of individual layers and the interaction between layers has some undefined effect on the resultant electronic structure of the entire particle. Once understood, these interactions will undoubtedly prove to be non-trivial.

The compositionally graded nanocrystals have demonstrated unique gradation-dependent optical properties. Observed improvements in optical performance are the most notable. Fluctuations in optical absorption, photoluminescence and quantum yields are observed by inducing a change in the rate of reactivity of precursors and are thought to be due to disparate charge distributions from radially changing sulfur concentrations. Atypical of binary semiconductor nanocrystals and homogeneous alloys, absorption and photoluminescence of gradient nanocrystals do not demonstrate a red-shift with growing diameter nor are optical wavelengths continually affected by changing stoichiometries. The exception to the previous statement is the observation of increased quantum yields

that are dependent on the degree of gradation. The highest quantum yield observed is 74%. In view of the changing quantum yields with varying degrees of gradation and earlier reports of blinking suppression[55], semiconductor nanocrystals with chemical composition gradients may prove to be model systems for studying and identifying specific non-radiative processes associated with luminescent efficiency and fluorescence intermittency.

Further studies are needed to explicate on the dependence of electronic structure and optical properties on the internal structure and gradation of compositionally gradient nanocrystals. To do so with CdSSe, more detailed correlations between optical properties and gradation are needed to elucidate the true nature of the phenomena observed here and to better understand the effects of gradation on quantum confinement with the nanocrystals. Explorations in material synthesis should continue. Substituting varying S and Se complexes as anionic precursors should induce internal structures and gradation effects that have not yet been observed. These novel gradation effects are possible simply because of the sensitivity of the experiment to changing parameters. The rate of reaction for each precursor is material specific and also affected by other reactants and reactant concentrations.

Additional chemistries of compositionally graded nanocrystals were fabricated (i.e. Zn and Pb gradient systems) and should be studied to unveil the effects of inducing inhomogeneous internal structures with varying chemistries. Just as enhanced optical properties were observed in these experiments, gradient nanocrystalline structures may exhibit novel electronic and magnetic phenomena that are dependent on their chemical composition and structural configuration.

In addition, XRD data should be scrutinized and evaluated as a complimentary technique to characterizing gradient effects on the crystal structures of the materials. With known nanocrystal diameters and size dispersions, investigations into line broadening and non-uniform peak shifts and their departure from parent, bulk crystal structures should offer a plethora of new and complimentary information regarding internal structures and gradation.

Currently, the technology to image the internal structure of the gradient nanocrystals on the Angstrom scale does not exist and may never. Nonetheless, it is imperative to develop a working model or some visualization of the internal structure of these materials. To do so accurately, some insight into the growth process and gradation effects on the physical properties of the materials is needed. A theoretical approach to evaluating and discovering the potential of gradient nanocrystals is necessary.

APPENDIX

A. Additional Compositionally Graded Semiconducting Nanocrystal Materials

Enhancements in photophysical properties, as described in Chapter III, are expected due to the structural variations associated with chemical composition grading and are not particular to the chemistries of the materials. Some correlation can be made between the type of atom chosen for substitution in the gradient alloy and the velocity of enhancement. Ternary alloys are formed when atoms of a chosen element are incorporated into a binary structure and crystallize as the chosen element substitutes the corresponding cation or anion in the crystal matrix. Gradient materials crystallize in a similar fashion only with non-uniform stoichiometries at varying depths. For gradient structures, resultant photophysical properties are greatly dependent on whether the substitutional atom is an anion or cation. As mentioned previously, some of the factors associated with enhancements in photophysical properties in gradient alloys are as follows: 1) distorted lattice constants, (2) deformation of electron distribution due to the differences in electronegativity of constituent atoms, and (3) variations in anion – cation bond lengths. The ionic type of the substitutional atom directly affects the degree of distortion in lattice constants and the crystal matrix; also, it would directly affect the electron distributions as anions tend to be more electronegative and cause larger distortions. Previous, gradient CdSSe nanocrystals were discussed in which substitutional atoms were anions. This section explores gradient nanocrystals in which substitutional atoms are cations.

A.1 On the Optical Properties of Compositionally Graded CdZnSe Nanocrystals

Nanocrystals of compositionally gradient CdZnSe were synthesized according to procedures found in Section 2.2.2 of this document. Similar to the case of compositionally graded CdSSe nanocrystals, RBS analysis (Figure A1) of CdZnSe reveal the gradient nature of the as-synthesized CdZnSe nanocrystals as the Cd:Zn atomic ratio varies with growth time.

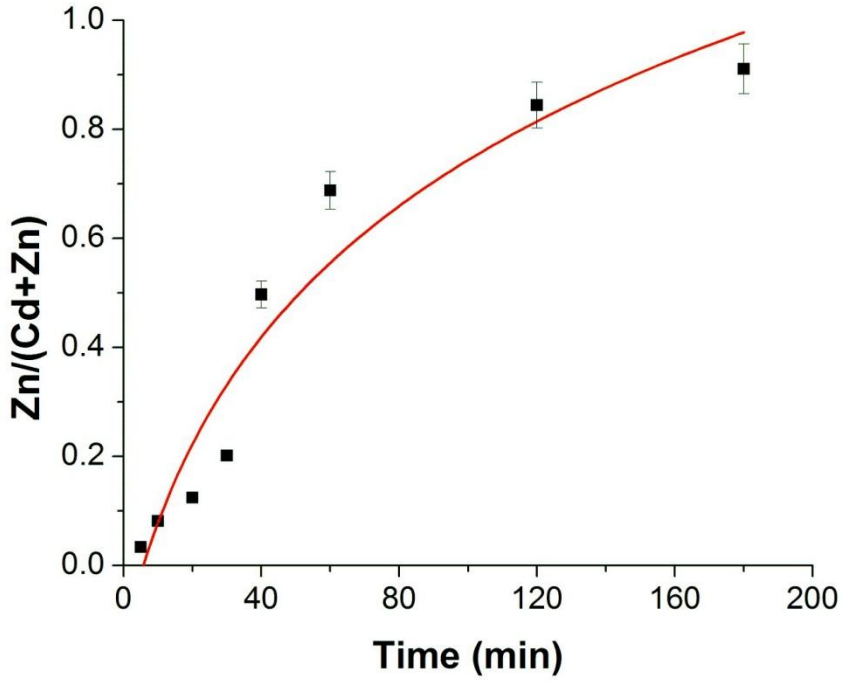

Figure A1. RBS analysis of nanocrystal stoichiometry as a function of growth time for CdSbSe nanocrystals. Graphs depict changing chemical composition of Zn with growth time. The gradual increase in zinc content with growth time indicates that these CdZnSe nanocrystals are grown with a chemical composition gradient where there is a Cd-rich core and Zn-rich shell.

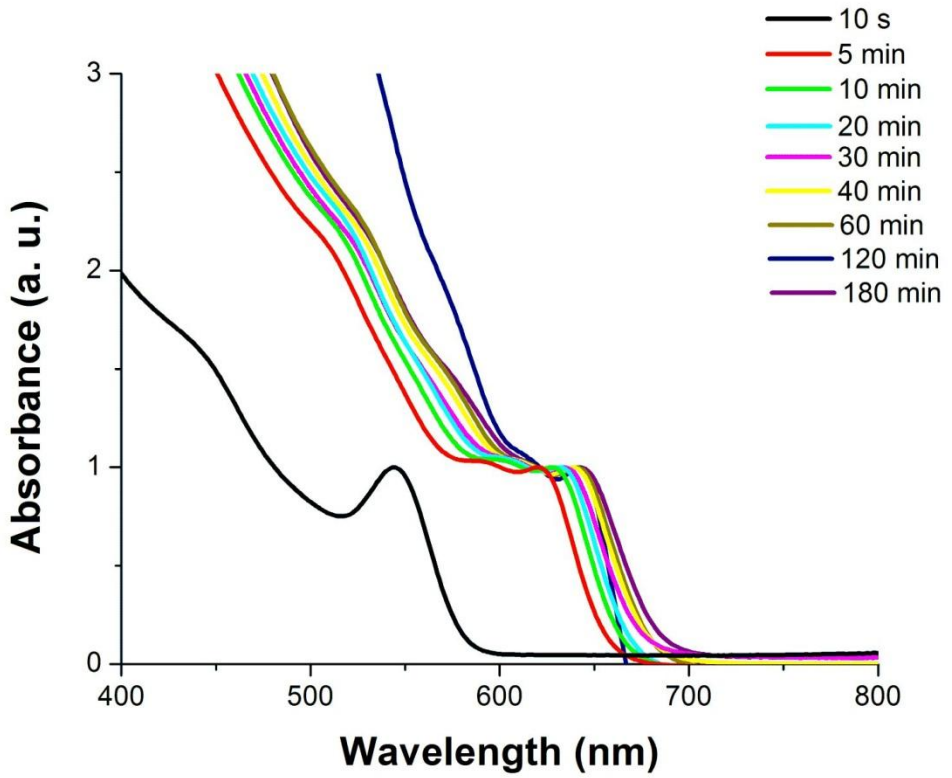

Figure A2. Optical absorption spectra of compositionally graded CdZnSe nanocrystals at varying growth times.

Also, similar to the case of compositionally graded CdSSe nanocrystals, a red shift in absorption is observed with increasing growth times. As concentrations of Zn increase, absorption red shifts to longer wavelengths, then remains unchanged with longer growth times. Photoluminescence is not reported here for gradient CdZnSe nanocrystals considering initial experiments yielded zero luminescence. Further exploration of this material is needed to explore the lack of luminescent output. Core/shell materials of CdZnSe typically yield high luminescence[80,81,82].

A.2 On the Morphology of Compositionally Graded CdPbSe Nanocrystals

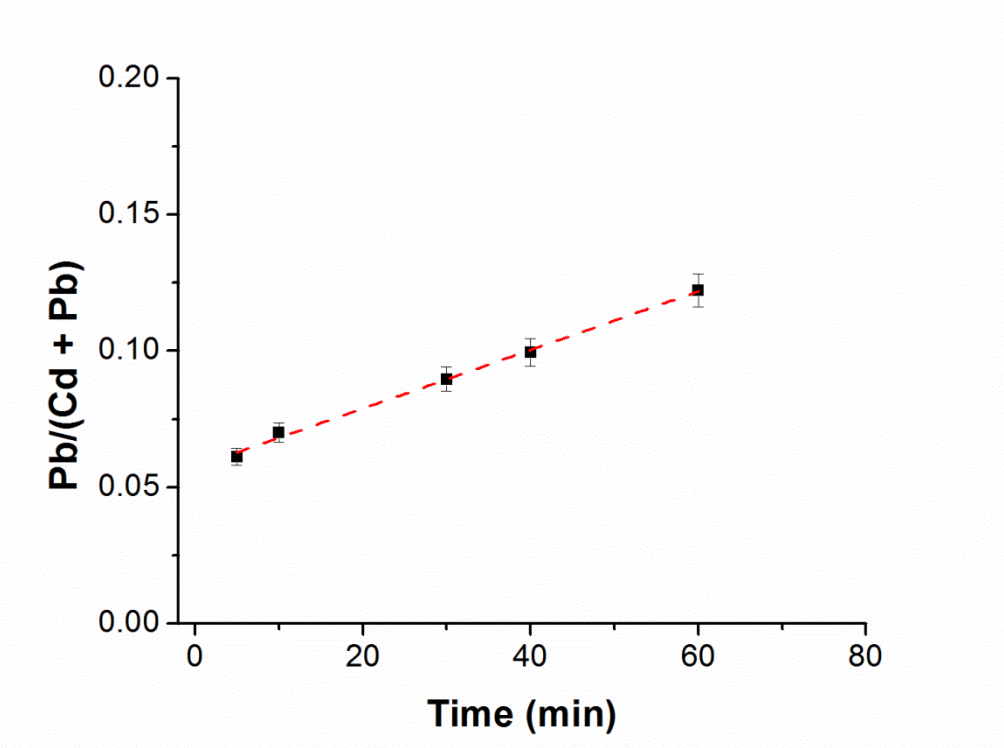

Figure A3. Graphical analysis of RBS data of CdPbSe depicts changing chemical composition of Pb with growth time. The gradual increase in sulfur content with growth time indicates that these CdPbSe nanocrystals are grown with a chemical composition gradient where there is a Cd-rich core and Pb-rich shell.

RBS was used to analyze chemical compositions of CdPbSe nanomaterials with growth time. Stoichiometric ratios of cationic components are presented in Figure A3. Gradient CdPbSe nanomaterials show increasing concentrations of Pb with growth time. TEM micrographs of the CdPbSe nanomaterials were analyzed and show morphologies deviant from that of CdSSe gradient nanocrystals (Figure A4). Initially, the boomerang-like morphologies of CdPbSe gradient nanomaterials were thought to be due to the large mismatch in ionic radii of both Cd^{2+} and Pb^{2+}. Upon closer inspection and in obtaining high resolution TEM micrographs (Figure A5) of these nanomaterials, it appears as if the

gradient CdPbSe materials crystallize in a distorted spherical form then assemble into boomerang-like structures. We were able to isolate one of these structures in a high resolution image (Figure A6). The crystallographic fringe pattern visible in Figure A6 shows a continuous crystal structure but with extensive twinning. Further studies on the crystallographic effects of inducing chemical composition gradients in CdPbSe materials are necessary to understand this phenomenon.

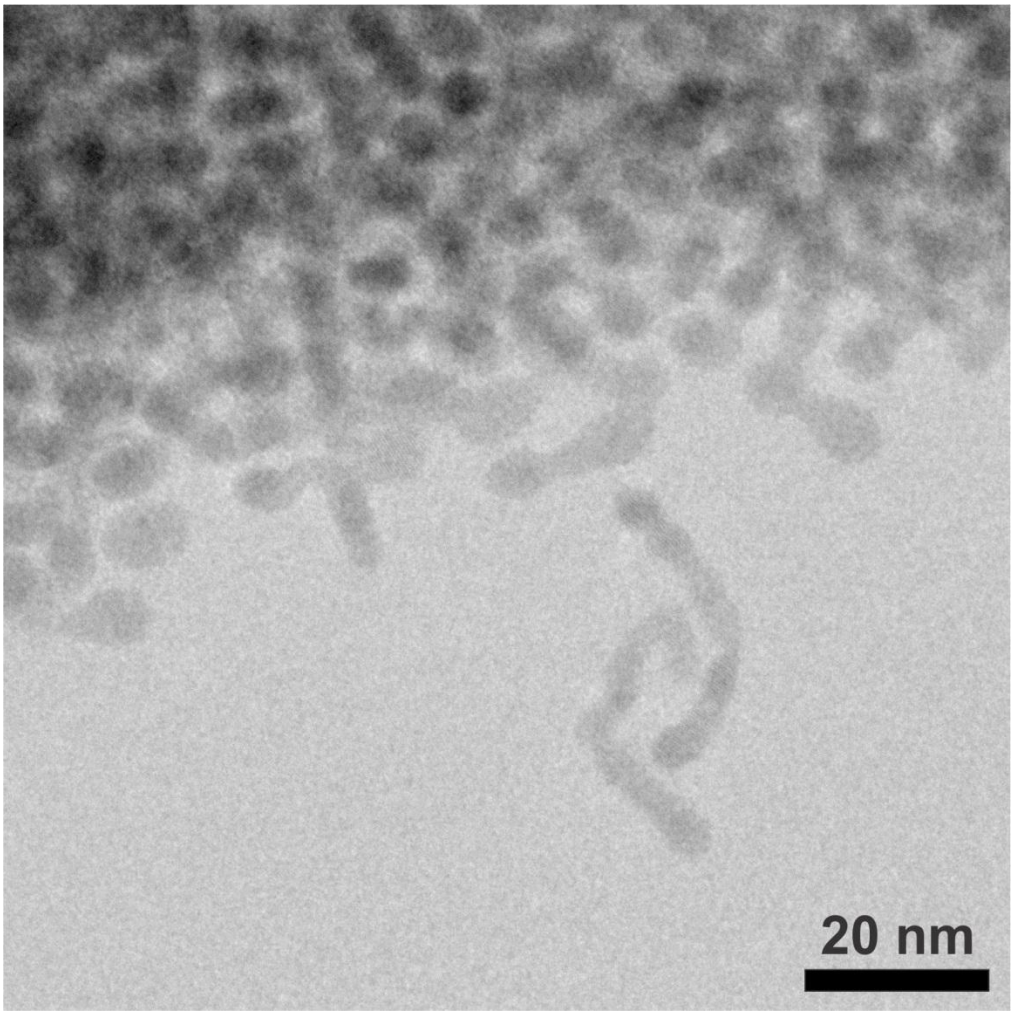

Figure A4. TEM micrograph of compositionally graded CdPbSe nanomaterials.

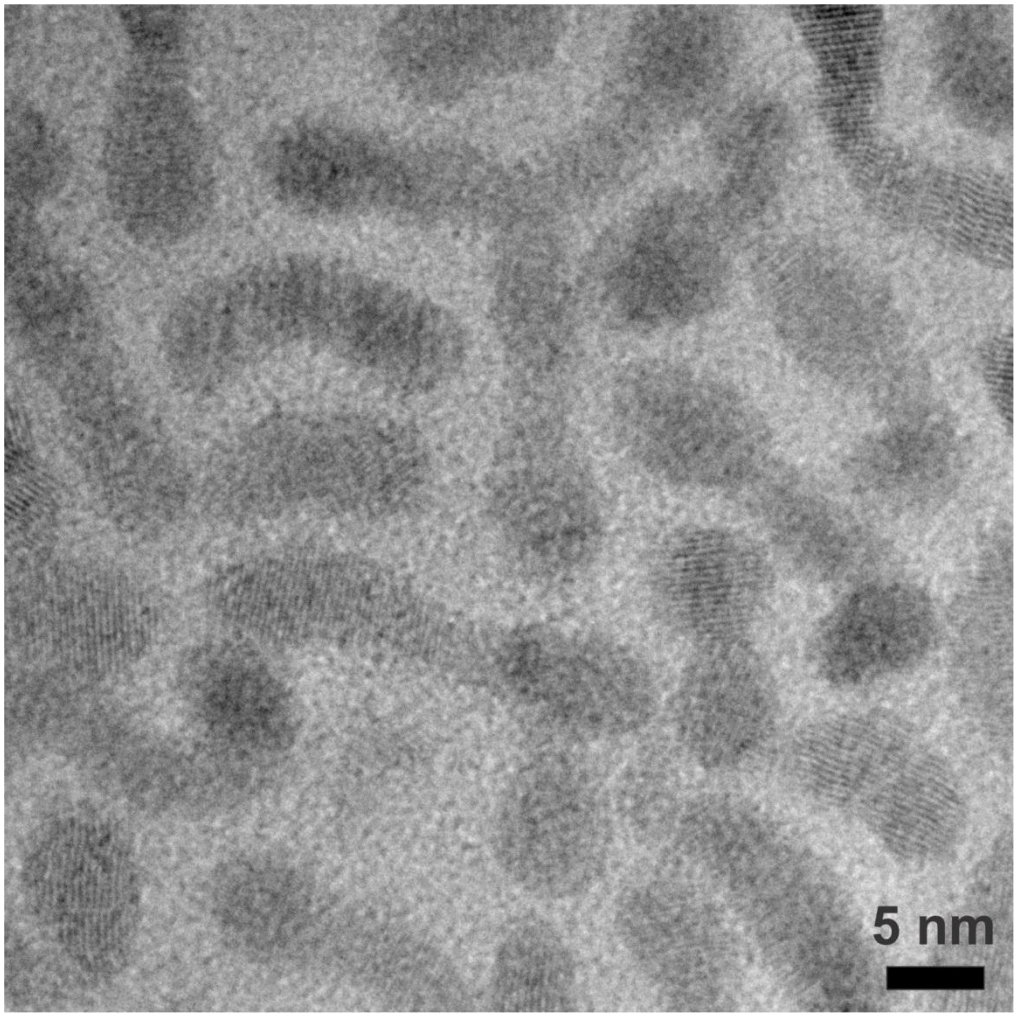

Figure A5. High resolution TEM micrograph of compositionally graded CdPbSe nanomaterials.

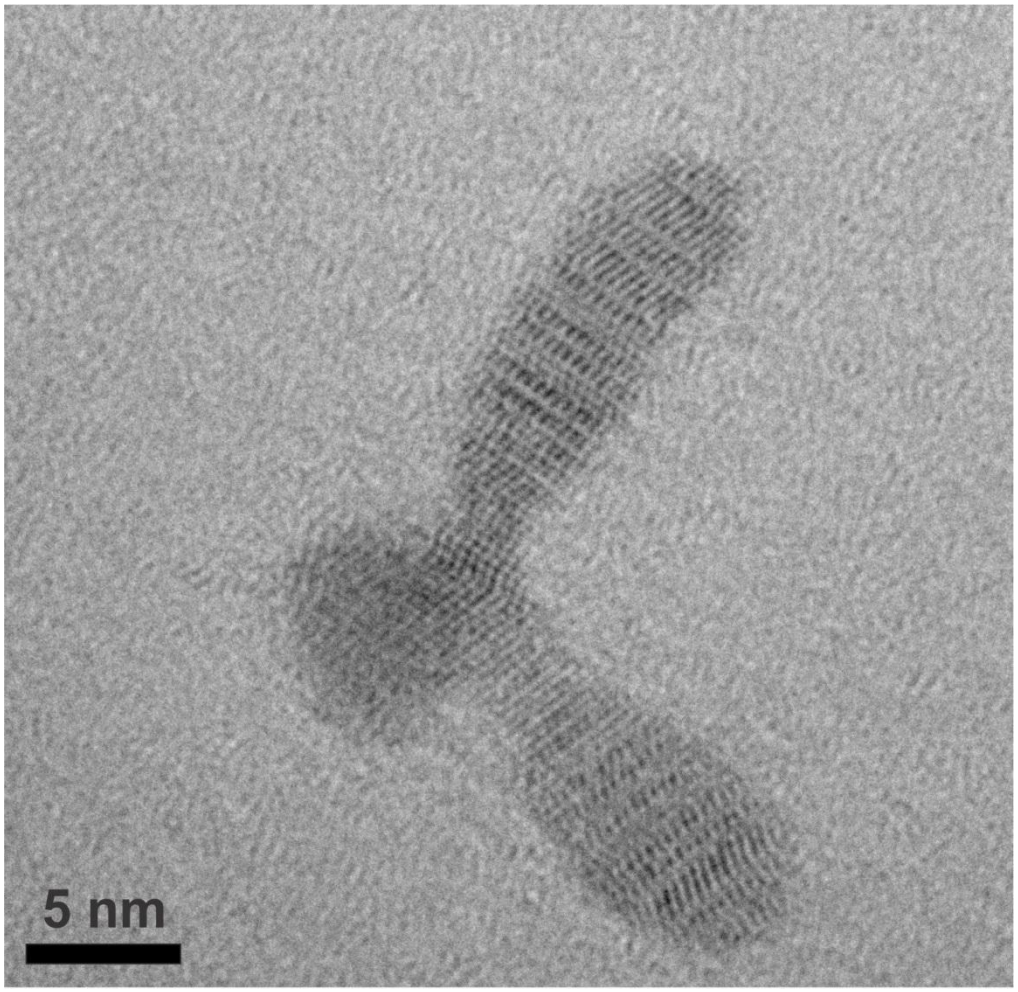

Figure A6. High resolution TEM micrograph of compositionally graded CdPbSe nanomaterials.

REFERENCES

1. Qingshan Li, W. H., Jing Sun, Jun Liu, Wei'an Yu, Zhubai Liu, Guangzhong Xing, Thinking Innovative Approaches and Materials Innovative Practice. *Advanced Materials Research* **2012,** *427*, 259-264.

2. Alivisatos, A. P., Semiconductor Clusters, Nanocrystals, and Quantum Dots. *Science* **1996,** *271* (5251), 933-937.

3. Brus, L., Quantum crystallites and nonlinear optics. *Applied Physics A: Materials Science & Processing* **1991,** *53* (6), 465-474.

4. Bawendi, M. G.; Steigerwald, M. L.; Brus, L. E., The Quantum Mechanics of Larger Semiconductor Clusters ("Quantum Dots"). *Annual Review of Physical Chemistry* **1990,** *41* (1), 477-496.

5. Takagahara, T.; Takeda, K., Theory of the quantum confinement effect on excitons in quantum dots of indirect-gap materials. *Physical Review B* **1992,** *46* (23), 15578-15581.

6. Yu, H.; Li, J.; Loomis, R. A.; Wang, L.-W.; Buhro, W. E., Two- versus three-dimensional quantum confinement in indium phosphide wires and dots. *Nat Mater* **2003,** *2* (8), 517-520.

7. Cossairt, B. M.; Owen, J. S., CdSe Clusters: At the Interface of Small Molecules and Quantum Dots. *Chemistry of Materials* **2011,** *23* (12), 3114-3119.

8. Nirmal, M.; Brus, L., Luminescence Photophysics in Semiconductor Nanocrystals. *Accounts of Chemical Research* **1998,** *32* (5), 407-414.

9. Albe, V.; Jouanin, C.; Bertho, D., Confinement and shape effects on the optical spectra of small CdSe nanocrystals. *Physical Review B* **1998,** *58* (8), 4713-4720.

10. Manna, L.; Scher, E. C.; Alivisatos, A. P., Synthesis of Soluble and Processable Rod-, Arrow-, Teardrop-, and Tetrapod-Shaped CdSe Nanocrystals. *Journal of the American Chemical Society* **2000,** *122* (51), 12700-12706.

11. Mano, T.; Kuroda, T.; Sanguinetti, S.; Ochiai, T.; Tateno, T.; Kim, J.; Noda, T.; Kawabe, M.; Sakoda, K.; Kido, G.; Koguchi, N., Self-Assembly of Concentric Quantum Double Rings. *Nano Letters* **2005,** *5* (3), 425-428.

12. Hines, M. A.; Guyot-Sionnest, P., Synthesis and Characterization of Strongly Luminescing ZnS-Capped CdSe Nanocrystals. *The Journal of Physical Chemistry* **1996,** *100* (2), 468-471.

13. (a) Bae, W. K.; Kwak, J.; Park, J. W.; Char, K.; Lee, C.; Lee, S., Highly Efficient Green-Light-Emitting Diodes Based on CdSe@ZnS Quantum Dots with a Chemical-Composition Gradient. *Advanced Materials* **2009,** *21* (17), 1690-1694; (b) Zhao, J.; Bardecker, J. A.; Munro, A. M.; Liu, M. S.; Niu, Y.; Ding, I. K.; Luo, J.; Chen, B.; Jen, A. K. Y.; Ginger, D. S., Efficient CdSe/CdS Quantum Dot Light-Emitting Diodes Using a Thermally Polymerized Hole Transport Layer. *Nano Letters* **2006,** *6* (3), 463-467.

14. (a) Schreuder, M. A.; Xiao, K.; Ivanov, I. N.; Weiss, S. M.; Rosenthal, S. J., White Light-Emitting Diodes Based on Ultrasmall CdSe Nanocrystal Electroluminescence. *Nano Letters* **2010,** *10* (2), 573-576; (b) Bowers Ii, M. J.; McBride, J. R.; Garrett, M. D.; Sammons, J. A.; Dukes Iii, A. D.; Schreuder, M. A.; Watt, T. L.; Lupini, A. R.; Pennycook, S. J.; Rosenthal, S. J., Structure and Ultrafast Dynamics of White-Light-Emitting CdSe Nanocrystals. *Journal of the American Chemical Society* **2009,** *131* (16), 5730-5731; (c) Bowers, M. J.; McBride, J. R.; Rosenthal, S. J., White-Light Emission from Magic-Sized Cadmium Selenide Nanocrystals. *Journal of the American Chemical Society* **2005,** *127* (44), 15378-15379.

15. Kwak, J.; Bae, W. K.; Lee, D.; Park, I.; Lim, J.; Park, M.; Cho, H.; Woo, H.; Yoon, D. Y.; Char, K.; Lee, S.; Lee, C., Bright and Efficient Full-Color Colloidal Quantum Dot Light-Emitting Diodes Using an Inverted Device Structure. *Nano Letters* **2012,** *12* (5), 2362-2366.

16. Beydoun, D.; Amal, R.; Low, G.; McEvoy, S., Role of Nanoparticles in Photocatalysis. *Journal of Nanoparticle Research* **1999,** *1* (4), 439-458.

17. Zheng, Y.; Zheng, L.; Zhan, Y.; Lin, X.; Zheng, Q.; Wei, K., Ag/ZnO Heterostructure Nanocrystals: Synthesis, Characterization, and Photocatalysis. *Inorganic Chemistry* **2007,** *46* (17), 6980-6986.

18. Wang, C.; Kwon, K.-W.; Odlyzko, M. L.; Lee, B. H.; Shim, M., PbSe Nanocrystal/TiOx Heterostructured Films: A Simple Route to Nanoscale Heterointerfaces and Photocatalysis. *The Journal of Physical Chemistry C* **2007,** *111* (31), 11734-11741.

19. Bohle, D. S.; Spina, C. J., Cationic and Anionic Surface Binding Sites on Nanocrystalline Zinc Oxide: Surface Influence on Photoluminescence and Photocatalysis. *Journal of the American Chemical Society* **2009,** *131* (12), 4397-4404.

20. (a) Rosenthal, S. J.; Chang, J. C.; Kovtun, O.; McBride, J. R.; Tomlinson, I. D., Biocompatible Quantum Dots for Biological Applications. *Chemistry & Biology* **2011,** *18* (1), 10-24; (b) Rosenthal, S. J.; McBride, J.; Pennycook, S. J.; Feldman, L. C., Synthesis, surface studies, composition and structural characterization of CdSe, core/shell and biologically active nanocrystals. *Surface Science Reports* **2007,** *62* (4), 111-157.

21. Bruchez, M.; Moronne, M.; Gin, P.; Weiss, S.; Alivisatos, A. P., Semiconductor Nanocrystals as Fluorescent Biological Labels. *Science* **1998,** *281* (5385), 2013-2016.

22. Warnement, M. R.; Tomlinson, I. D.; Rosenthal, S. J., Fluorescent imaging applications of Quantum Dot probes. *Curr Nanosci* **2007,** *3* (4), 273-284.

23. Michalet, X.; Pinaud, F. F.; Bentolila, L. A.; Tsay, J. M.; Doose, S.; Li, J. J.; Sundaresan, G.; Wu, A. M.; Gambhir, S. S.; Weiss, S., Quantum Dots for Live Cells, in Vivo Imaging, and Diagnostics. *Science* **2005,** *307* (5709), 538-544.

24. Klimov, V. I.; Mikhailovsky, A. A.; Xu, S.; Malko, A.; Hollingsworth, J. A.; Leatherdale, C. A.; Eisler, H.-J.; Bawendi, M. G., Optical Gain and Stimulated Emission in Nanocrystal Quantum Dots. *Science* **2000,** *290* (5490), 314-317.

25. Eisler, H. J.; Sundar, V. C.; Bawendi, M. G.; Walsh, M.; Smith, H. I.; Klimov, V., Color-selective semiconductor nanocrystal laser. *Appl Phys Lett* **2002,** *80* (24), 4614-4616.

26. Que, W., Excitons in quantum dots with parabolic confinement. *Physical Review B* **1992,** *45* (19), 11036-11041.

27. Olkhovets, A.; Hsu, R. C.; Lipovskii, A.; Wise, F. W., Size-Dependent Temperature Variation of the Energy Gap in Lead-Salt Quantum Dots. *Physical Review Letters* **1998,** *81* (16), 3539-3542.

28. El-Sayed, M. A., Small Is Different: Shape-, Size-, and Composition-Dependent Properties of Some Colloidal Semiconductor Nanocrystals. *Accounts of Chemical Research* **2004,** *37* (5), 326-333.

29. Sapra, S.; Sarma, D. D., Evolution of the electronic structure with size in II-VI semiconductor nanocrystals. *Physical Review B* **2004,** *69* (12), 125304.

30. P. Y. Yu, M. C., *Fundamentals of Semiconductors*. 4th ed.; Springer: 2010.

31. Cardona, P. Y., *Fundamentals of semiconductors*. Springer 1996.

32. Klimov, V., *semiconductor and Metal Nanocrystals* 2004.

33. (a) Brus, L. E., A Simple-Model for the Ionization-Potential, Electron-Affinity, and Aqueous Redox Potentials of Small Semiconductor Crystallites. *Journal of Chemical Physics* **1983,** *79* (11), 5566-5571; (b) Brus, L. E., Electron Electron and Electron-Hole Interactions in Small Semiconductor Crystallites - the Size Dependence of the Lowest Excited Electronic State. *Journal of Chemical Physics* **1984,** *80* (9), 4403-4409.

34. Talapin, D. V.; Rogach, A. L.; Kornowski, A.; Haase, M.; Weller, H., Highly Luminescent Monodisperse CdSe and CdSe/ZnS Nanocrystals Synthesized in a Hexadecylamine−Trioctylphosphine Oxide−Trioctylphospine Mixture. *Nano Lett* **2001,** *1* (4), 207-211.

35. Schreuder, M. A.; McBride, J. R.; Dukes, A. D.; Sammons, J. A.; Rosenthal, S. J., Control of Surface State Emission via Phosphonic Acid Modulation in Ultrasmall CdSe Nanocrystals: The Role of Ligand Electronegativity. *The Journal of Physical Chemistry C* **2009,** *113* (19), 8169-8176.

36. Peng, X.; Schlamp, M. C.; Kadavanich, A. V.; Alivisatos, A. P., Epitaxial Growth of Highly Luminescent CdSe/CdS Core/Shell Nanocrystals with Photostability and Electronic Accessibility. *Journal of the American Chemical Society* **1997,** *119* (30), 7019-7029.

37. Talapin, D. V.; Mekis, I.; Götzinger, S.; Kornowski, A.; Benson, O.; Weller, H., CdSe/CdS/ZnS and CdSe/ZnSe/ZnS Core−Shell−Shell Nanocrystals. *The Journal of Physical Chemistry B* **2004,** *108* (49), 18826-18831.

38. Chen, Y.; Vela, J.; Htoon, H.; Casson, J. L.; Werder, D. J.; Bussian, D. A.; Klimov, V. I.; Hollingsworth, J. A., "Giant" Multishell CdSe Nanocrystal Quantum Dots with Suppressed Blinking. *Journal of the American Chemical Society* **2008,** *130* (15), 5026-5027.

39. Peng, X. G.; Schlamp, M. C.; Kadavanich, A. V.; Alivisatos, A. P., Epitaxial growth of highly luminescent CdSe/CdS core/shell nanocrystals with photostability and electronic accessibility. *Journal of the American Chemical Society* **1997,** *119* (30), 7019-7029.

40. Chen, X.; Lou, Y.; Samia, A. C.; Burda, C., Coherency Strain Effects on the Optical Response of Core/Shell Heteronanostructures. *Nano Letters* **2003,** *3* (6), 799-803.

41. Shen, H.; Zhou, C.; Xu, S.; Yu, C.; Wang, H.; Chen, X.; Li, L. S., Phosphine-free synthesis of Zn1-xCdxSe/ZnSe/ZnSexS1-x/ZnS core/multishell structures with bright and stable blue-green photoluminescence. *Journal of Materials Chemistry* **2011,** *21* (16), 6046-6053.

42. Bailey, R. E.; Nie, S., Alloyed Semiconductor Quantum Dots: Tuning the Optical Properties without Changing the Particle Size. *Journal of the American Chemical Society* **2003,** *125* (23), 7100-7106.

43. Van Vechten, J. A.; Bergstresser, T. K., Electronic Structures of Semiconductor Alloys. *Physical Review B* **1970,** *1* (8), 3351-3358.

44. Ouyang, J.; Vincent, M.; Kingston, D.; Descours, P.; Boivineau, T.; Zaman, M. B.; Wu, X.; Yu, K., Noninjection, One-Pot Synthesis of Photoluminescent Colloidal Homogeneously Alloyed CdSeS Quantum Dots. *The Journal of Physical Chemistry C* **2009,** *113* (13), 5193-5200.

45. The variation of the energy gap with composition in the quaternary alloy system ZnTe1−2xSxSex. *physica status solidi (b)* **1983,** *115* (2), K151.

46. Regulacio, M. D.; Han, M.-Y., Composition-Tunable Alloyed Semiconductor Nanocrystals. *Accounts of Chemical Research* **2010,** *43* (5), 621-630.

47. Deng, Z.; Yan, H.; Liu, Y., Band Gap Engineering of Quaternary-Alloyed ZnCdSSe Quantum Dots via a Facile Phosphine-Free Colloidal Method. *Journal of the American Chemical Society* **2009,** *131* (49), 17744-17745.

48. Bae, W. K.; Char, K.; Hur, H.; Lee, S., Single-Step Synthesis of Quantum Dots with Chemical Composition Gradients. *Chemistry of Materials* **2008,** *20* (2), 531-539.

49. Liu, N.; Tersoff, J.; Baklenov, O.; Holmes, A. L., Jr.; Shih, C. K., Nonuniform Composition Profile in In_{0.5}Ga_{0.5}As Alloy Quantum Dots. *Physical Review Letters* **2000,** *84* (2), 334-337.

50. Sun, H.; Zhang, H.; Ju, J.; Zhang, J.; Qian, G.; Wang, C.; Yang, B.; Wang, Z. Y., One-Step Synthesis of High-Quality Gradient CdHgTe Nanocrystals: A Prerequisite to Prepare CdHgTe−Polymer Bulk Composites with Intense Near-Infrared Photoluminescence. *Chemistry of Materials* **2008,** *20* (21), 6764-6769.

51. Swafford, L. A.; Weigand, L. A.; Bowers, M. J.; McBride, J. R.; Rapaport, J. L.; Watt, T. L.; Dixit, S. K.; Feldman, L. C.; Rosenthal, S. J., Homogeneously Alloyed CdSxSe1-x Nanocrystals: Synthesis, Characterization, and Composition/Size-Dependent Band Gap. *Journal of the American Chemical Society* **2006,** *128* (37), 12299-12306.

52. Glisson, T.; Hauser, J.; Littlejohn, M.; Williams, C., Energy bandgap and lattice constant contours of iii–v quaternary alloys. *Journal of Electronic Materials* **1978,** *7* (1), 1-16.

53. Bellaiche, L.; Wei, S.-H.; Zunger, A., Composition dependence of interband transition intensities in GaPN, GaAsN, and GaPAs alloys. *Physical Review B* **1997,** *56* (16), 10233-10240.

54. Chen, Y.; Vela, J.; Htoon, H.; Casson, J. L.; Werder, D. J.; Bussian, D. A.; Klimov, V. I.; Hollingsworth, J. A., "Giant" multishell CdSe nanocrystal quantum dots with suppressed blinking. *Journal of the American Chemical Society* **2008,** *130* (15), 5026-+.

55. Wang, X.; Ren, X.; Kahen, K.; Hahn, M. A.; Rajeswaran, M.; Maccagnano-Zacher, S.; Silcox, J.; Cragg, G. E.; Efros, A. L.; Krauss, T. D., Non-blinking semiconductor nanocrystals. *Nature* **2009,** *459* (7247), 686-689.

56. McBride, J.; Treadway, J.; Feldman, L. C.; Pennycook, S. J.; Rosenthal, S. J., Structural Basis for Near Unity Quantum Yield Core/Shell Nanostructures. *Nano Letters* **2006,** *6* (7), 1496-1501.

57. Park, J.; An, K.; Hwang, Y.; Park, J.-G.; Noh, H.-J.; Kim, J.-Y.; Park, J.-H.; Hwang, N.-M.; Hyeon, T., Ultra-large-scale syntheses of monodisperse nanocrystals. *Nat Mater* **2004,** *3* (12), 891-895.

58. Harrison, M. A. N., A; Rosenthal, S. J, CdSSe Nanocrystals with Induced Chemical Composition Gradients. *Israel Journal of Chemistry* **2012**, accepted.

59. Langford, J. I.; Wilson, A. J. C., Scherrer after sixty years: A survey and some new results in the determination of crystallite size. *Journal of Applied Crystallography* **1978,** *11* (2), 102-113.

60. Erwin, M. M.; McBride, J.; Kadavanich, A. V.; Rosenthal, S. J., Effects of impurities on the optical properties of poly-3-hexylthiophene thin films. *Thin Solid Films* **2002,** *409* (2), 198-205.

61. Bevington, P. R., Data Reduction and Error Analysis for the Physical Sciences. McGraw-Hill: New York, 1969.

62. Feldman, L. C. M., J.W., *Fundamentals of Surface and Thin Film Analysis*. North Holland-Elsevier: New York, 1986.

63. Bäumler, W.; Penzkofer, A., Fluorescence spectroscopic analysis of N and P isomers of DODCI. *Chemical Physics* **1990,** *140* (1), 75-97.

64. Taylor, J.; Kippeny, T.; Rosenthal, S. J., Surface Stoichiometry of CdSe Nanocrystals Determined by Rutherford Backscattering Spectroscopy. *Journal of Cluster Science* **2001,** *12* (4), 571-582.

65. Li, J. J.; Wang, Y. A.; Guo, W.; Keay, J. C.; Mishima, T. D.; Johnson, M. B.; Peng, X., Large-Scale Synthesis of Nearly Monodisperse CdSe/CdS Core/Shell Nanocrystals Using Air-Stable Reagents via Successive Ion Layer Adsorption and Reaction. *Journal of the American Chemical Society* **2003,** *125* (41), 12567-12575.

66. Denton, A. R.; Ashcroft, N. W., Vegard's law. *Physical Review A* **1991,** *43* (6), 3161-3164.

67. Vegard, L., Die Konstitution der Mischkristalle und die Raumfüllung der Atome. *Zeitschrift für Physik A Hadrons and Nuclei* **1921,** *5* (1), 17-26.

68. Ouyang, J.; Zaman, M. B.; Yan, F. J.; Johnston, D.; Li, G.; Wu, X.; Leek, D.; Ratcliffe, C. I.; Ripmeester, J. A.; Yu, K., Multiple Families of Magic-Sized CdSe Nanocrystals with Strong Bandgap Photoluminescence via Noninjection One-Pot Syntheses. *The Journal of Physical Chemistry C* **2008,** *112* (36), 13805-13811.

69. Wickham, J. N.; Herhold, A. B.; Alivisatos, A. P., Shape Change as an Indicator of Mechanism in the High-Pressure Structural Transformations of CdSe Nanocrystals. *Physical Review Letters* **2000,** *84* (5), 923-926.

70. Soumare, Y.; Piquemal, J. Y.; Maurer, T.; Ott, F.; Chaboussant, G.; Falqui, A.; Viau, G., Oriented magnetic nanowires with high coercivity. *Journal of Materials Chemistry* **2008,** *18* (46), 5696-5702.

71. Durose, K.; Fellows, A. T.; Brinkman, A. W.; Russell, G. J.; Woods, J., Structural aspects of ball milled CdS and CdSe. *Journal of Materials Science* **1985,** *20* (10), 3783-3789.

72. Jiang, Z.-J.; Kelley, D. F., Role of Magic-Sized Clusters in the Synthesis of CdSe Nanorods. *ACS Nano* **2010,** *4* (3), 1561-1572.

73. Riehle, F. S.; Bienert, R.; Thomann, R.; Urban, G. A.; Krüger, M., Blue Luminescence and Superstructures from Magic Size Clusters of CdSe. *Nano Letters* **2009,** *9* (2), 514-518.

74. Zunger, A.; Jaffe, J. E., Structural Origin of Optical Bowing in Semiconductor Alloys. *Physical Review Letters* **1983,** *51* (8), 662-665.

75. (a) Bernard, J. E.; Zunger, A., Optical bowing in zinc chalcogenide semiconductor alloys. *Physical Review B* **1986,** *34* (8), 5992-5995; (b) -Resolved Alloy Bowing in Pseudobinary InGaAs Alloys. *Physical Review Letters* **1988,** *61* (7), 877.

76. Wang, X. Y.; Ren, X. F.; Kahen, K.; Hahn, M. A.; Rajeswaran, M.; Maccagnano-Zacher, S.; Silcox, J.; Cragg, G. E.; Efros, A. L.; Krauss, T. D., Non-blinking semiconductor nanocrystals. *Nature* **2009,** *459* (7247), 686-689.

77. Landolt, H., *Landolt-Bornstein: Numerical Data and Functional Relationships in Science and Technology*. Springer: New York, 1982; Vol. III-17b.

78. Vektaris, G., A new approach to the molecular biexciton theory. *The Journal of Chemical Physics* **1994,** *101* (4), 3031-3040.

79. Swafford, L. A. Homogeneously Alloyed Cadmium Sulfoselenide Nanocrystals. Vanderbilt University, 2006.

80. Danek, M.; Jensen, K. F.; Murray, C. B.; Bawendi, M. G., Synthesis of Luminescent Thin-Film CdSe/ZnSe Quantum Dot Composites Using CdSe Quantum Dots Passivated with an Overlayer of ZnSe. *Chemistry of Materials* **1996,** *8* (1), 173-180.

81. Reiss, P.; Bleuse, J.; Pron, A., Highly Luminescent CdSe/ZnSe Core/Shell Nanocrystals of Low Size Dispersion. *Nano Letters* **2002,** *2* (7), 781-784.

82. Reiss, P.; Carayon, S.; Bleuse, J.; Pron, A., Low polydispersity core/shell nanocrystals of CdSe/ZnSe and CdSe/ZnSe/ZnS type: preparation and optical studies. *Synthetic Metals* **2003,** *139* (3), 649-652.

LIST OF PUBLICATIONS

1. **M. A. Harrison**, A. Ng, S. J. Rosenthal, "Alloyed CdSSe Nanocrystals with Induced Chemical Composition Gradient", *Israel Journal of Chemistry*, Special Issue: Nanochemistry (2012), accepted.

2. J. S. Niezgoda, **M. A. Harrison**, J. R. McBride, S. J. Rosenthal, "Novel Synthesis of Chalcopyrite $Cu_xIn_yS_2$ Quantum Dots with Tunable Localized Surface Plasmon Resonance", *Chemistry of Materials* 24, 3294-3298 (2012).

3. S. Somarajan, **M. A. Harrison**, D. S. Koktysh, W. He, S. A. Hasan, J. Park, R. L. Stillwll, E. A. Payzant, J. H. Dickerson, "Structural and magnetic analysis of nanocrystalline lead europium sulfide (PbxEuyS)", *Materials Chemistry and Physics* 134, 1-6 (2012).

4. **M. A. Harrison**, S. Somarajan, S. V. Mahajan, D. S. Koktysh, K. van Benthem and J. H. Dickerson, "Template Assisted Synthesis of EuS Nanotubes", *Materials Letters* 65, 420 (2011).

5. D. S. Koktysh, S. Somarajan, W. He, **M. A. Harrison**, S. A. McGill and J. H. Dickerson, "EuS nanocrystals: a novel synthesis for the generation of mondisperse nanocrystals with size-dependent optical properties", *Nanotechnology* 21, 415601 (2010).

6. S. Somarajan, S. A. Hasan, **M. A. Harrison**, S. V. Mahajan, C. T. Adkins, E. Harth and J. H. Dickerson, "Electrophoretic Deposition of Star Polymer-Europium Chalcogenide Nanocomposite Films", *Key Engineering Materials* 412, 113-118 (2009).

7. A. Thron, C.S. Bonifacio, N. Erdman, **M. A. Harrison**, S. Somarajan, J. H. Dickerson, K. van Benthem,, "Characterization of EuS Nanotubes in Quantum Confinement", *Microscopy and Microanalysis* 15, 1178-1179 (2009).